Investigating a High-Order Viscous Flux Scheme for Unstructured Grids

Florian Setzwein* and Peter Ess†
Institute of Combustion Technology, German Aerospace Center (DLR), Stuttgart, 70569, Germany
and
Peter Gerlinger‡
IVLR, University of Stuttgart, Stuttgart, 70569, Germany

https://doi.org/10.2514/1.J064132

A viscous flux formulation at interior faces and at Dirichlet boundary conditions in the framework of unstructured vertex-centered k-exact finite-volume schemes is presented. It is based on a geometric decomposition of the viscous flux into orthogonal and nonorthogonal parts. Special emphasis is put on the truncation errors and the spectral properties of the scheme, and a connection is established to the well-known α-damping scheme. The latter is also used to introduce discretization coefficients into the method that allow a fourth and a sixth order of accuracy in space on Cartesian grids. The effect of the scheme is presented in terms of canonical diffusion problems, as well as test cases for laminar wall-bounded flows. It is shown that the method preserves a second-order accuracy for the viscous operator, even on highly distorted unstructured grids and in the presence of boundaries and that it strongly enhances the solution accuracy with respect to a conventional scheme for viscous fluxes.

I. Introduction

HIGH-ORDER schemes for unstructured grids offer great capabilities for the reduction of computation time for detailed large-eddy simulations, while maintaining a large geometric flexibility in the mesh generation process [1]. Promising approaches, such as the discontinuous Galerkin method [2–5] or the spectral volume method [6–9] offer a higher order of accuracy on unstructured grids by introducing additional degrees of freedom within computational elements. Unfortunately, implementing such schemes into established finite-volume flow solvers, which often include many complex models, is not a trivial task and requires a high verification and validation effort. A promising approach to improve unstructured state-of-the-art finite-volume solvers with a higher spatial accuracy is the k-exact multiple-correction approach by Pont et al. [10,11]. Its key is a successive correction of approximate Green–Gauss derivatives, which enables a high-order reconstruction with favorable parallel scaling properties and low implementation effort. The original cell-centered method has recently been extended to vertex-centered median-dual grids in combination with an implicit fractional step scheme for the solution of the Navier–Stokes equations [12]. Besides that, a novel central convective flux approximation has been proposed that is based on an adaptive dissipation control in order to achieve a stable solution with a minimum amount of numerical dissipation and without a tedious search for optimum empirical simulation parameters [13]. However, the former works did not account for a k-exact treatment of viscous fluxes in the vicinity of wall boundaries.

Chamarthi et al. [14,15] showed that the viscous flux discretization plays a major role for simulations on marginally resolved grids. In particular, it was emphasized that schemes, which fall into the category of the so-called α-damping approach, have particularly good spectral properties and produce significantly better numerical results than other high-order methods with a poor resolution on the high wavenumber side. The α-damping scheme is based on the work of Nishikawa [16] and is derived from an upwind advection scheme, which is applied to a fist-order hyperbolic relaxation system for diffusion. The method provides a degree of freedom (denoted α), which controls the spectral properties of the discretization scheme. It also influences the spatial truncation error, so that a fourth-order scheme on Cartesian grids can be realized by a suitable choice of α. In the work of Chamarthi [14], the method was extended by a further degree of freedom as part of a compact finite-difference approach, which allows the method to be extended to a sixth-order on Cartesian grids. Based on these extraordinary properties, the question arises of how this method can be accommodated within the k-exact multi-correction method on vertex-centered grids.

In contrast to the derivation of the α-damping scheme, our approach is based on a geometric decomposition of the viscous fluxes, similar to the well-known scheme by Mathur and Murthy [17]. The latter is often used in combination with a finite-volume discretization on unstructured grids. The advantage of this derivation is that it can easily be applied to different k-exact reconstruction degrees and for the discretization of viscous fluxes at Dirichlet boundaries. We show how this approach can be turned into the α-damping scheme by introducing certain discretization coefficients, which, in analogy to the work of Nishikawa [16] and Chamarthi [14], can be used to control the spectral behavior and the spatial truncation errors of the scheme. Based on this analogy, special coefficients are derived, for which a fourth-order accuracy can be generated with a one-exact reconstruction and a sixth-order accuracy with a two-exact reconstruction on Cartesian grids. Additionally, the error properties of the geometrically derived method are highlighted, which exhibits second-order accuracy in space for both $k = 1$ and $k = 2$ even on truly unstructured grids.

The novel flux formulation is applied to the implicit high-order k-exact multiple-correction scheme on vertex-centered grids [12,18,19], which is implemented in DLR's finite-volume flow solver ThetaCOM (turbulent heat release extension for TAU in its combustion version). The impact of the viscous flux calculation concerning the solution accuracy is examined on a variety of flow problems. First, canonical diffusion problems are used to verify the spatial error convergence with regards to different discretization coefficients. In particular, the influence of grid distortions on the error convergence is examined. The scheme is then used to simulate various laminar and turbulent, wall-bounded flow problems and is compared to the original scheme by Mathur and Murthy in terms of the spatial accuracy.

Presented as Paper 2024-2175 at the AIAA SciTech Forum and Exposition 2024, Orlando, FL, January 8–12, 2024; received 4 March 2024; revision received 7 July 2024; accepted for publication 6 August 2024; published online 30 September 2024.

*Postdoctoral Fellow; florian.setzwein@dlr.de (Corresponding Author).
†Postdoctoral Fellow. Senior Member AIAA.
‡Professor.

II. Numerical Methods

The following section gives a brief overview of the used k-exact multiple-correction approach for vertex-centered grids. The starting point is a general transport equation for a field variable ϕ that is convected in a fluid flow with velocity u_i and subject to diffusive transport with diffusivity D:

$$\frac{\partial \phi}{\partial t} + \frac{\partial}{\partial x_i}(u_i \phi) + \frac{\partial}{\partial x_i}\left(D \frac{\partial \phi}{\partial x_i}\right) = 0 \tag{1}$$

Equation (1) is solved with a finite-volume approach, where the computational domain Ω is divided into N nonoverlapping computational elements Ω_α. These elements are given by the median-dual representation of the tessellated domain. The latter is denoted as primary grid and consists of linear elements such as triangles or quadrilaterals in $2D$ and tetrahedra, hexahedra, prisms, or pyramids in $3D$. Figure 1 shows an exemplary median-dual representation of a two-dimensional grid. Two elements Ω_α and Ω_β are said to be adjacent if they share a common face $A_{\alpha\beta}$. The set $\{\beta_\alpha^{(1)}\}$ is referred to as the first neighborhood of an element Ω_α and it comprises all elements adjacent to it. Elements that are located at the domain boundary also comprise a set of points $\{\delta_\alpha\}$, which will be used to evaluate numerical boundary fluxes. For reasons of clarity, the respective element faces on which these points are located will be denoted by $A_{\alpha\delta}$.

Central to the finite-volume approach is the volume average $\overline{\phi}_\alpha$ of the considered field variable over Ω_α, which is defined by

$$\overline{\phi}_\alpha = \frac{1}{|\Omega_\alpha|} \iiint_{\Omega_\alpha} \phi(\boldsymbol{x}) \, \mathrm{d}V \tag{2}$$

The volume averaging is applied to the governing equation (1) to obtain a set of equations where the unknown volume averages $\overline{\phi}_\alpha$ act as degrees of freedom:

$$\frac{\partial \overline{\phi}_\alpha}{\partial t} + \frac{1}{|\Omega_\alpha|} \sum_{\beta \in \{\beta_\alpha^{(1)}\}} \left[F_C^{(\alpha\beta)} + F_D^{(\alpha\beta)}\right] + \frac{1}{|\Omega_\alpha|} \sum_{\delta \in \{\delta_\alpha\}} \left[F_C^{(\alpha\delta)} + F_D^{(\alpha\delta)}\right] = 0 \tag{3}$$

Here, the convective and diffusive fluxes are defined for all interior faces by

$$F_C^{(\alpha\beta)} \coloneqq \iint_{A_{\alpha\beta}} u_i \phi n_i \, \mathrm{d}A \quad \text{and} \quad F_D^{(\alpha\beta)} \coloneqq \iint_{A_{\alpha\beta}} D \frac{\partial \phi}{\partial x_i} n_i \, \mathrm{d}A \tag{4}$$

and vice versa for fluxes across boundary faces $A_{\alpha\delta}$, where n_i denotes the unit normal vector. The goal of any finite-volume scheme is the approximation of these fluxes in terms of the volume averages $\overline{\phi}_\alpha$ to close the system of equations and proceed to a new time step. In this work, we use a k-exact reconstruction approach for this task, where the solution in the vicinity of an element Ω_α is locally approximated by a Taylor polynomial $\phi^{(k+1)}(\boldsymbol{x}; \boldsymbol{x}_\alpha)$ of degree k:

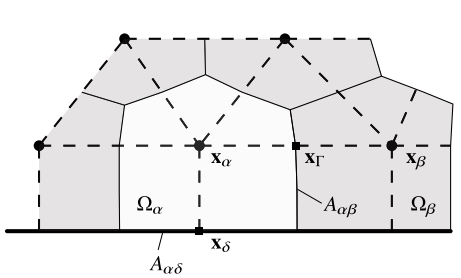

Fig. 1 Median-dual grid in 2D, indicated in solid lines. The corresponding primary grid is drawn in dashed lines. The simulation variables are stored at the location of primary grid nodes, that is, x_α or x_β.

$$\phi^{(k+1)}(\boldsymbol{x}; \boldsymbol{x}_\alpha) = \phi\Big|_{\boldsymbol{x}_\alpha}^{(k+1)} + \frac{\partial \phi}{\partial x_{i_1}}\Big|_{\boldsymbol{x}_\alpha}^{(k)} \left(x_{i_1} - x_{i_1,\alpha}\right) + \cdots + \frac{1}{k!} \frac{\partial^k \phi}{\partial x_{i_1} \ldots \partial x_{i_k}}\Big|_{\boldsymbol{x}_\alpha}^{(1)} \left(x_{i_1} - x_{i_1,\alpha}\right) \ldots \left(x_{i_k} - x_{i_k,\alpha}\right) \tag{5}$$

The point $\boldsymbol{x}_\alpha$ marks a vertex of the underlying primary grid structure, around which the median-dual element Ω_α is constructed and at which the volume average $\overline{\phi}_\alpha$ is stored. The value $\phi|_{\boldsymbol{x}_\alpha}^{(k+1)}$ denotes the approximation of the point value $\phi(\boldsymbol{x}_\alpha)$ with an accuracy of $\mathcal{O}(h^{k+1})$, where h refers to the local grid scale. In a similar fashion, the nth derivative term refers to an approximation of the true point-valued derivative of ϕ at $\boldsymbol{x}_\alpha$ with an accuracy of $\mathcal{O}(h^{k-n+1})$. The k-exact reconstruction approach aims to determine these unknown polynomial coefficients in such a way that the respective accuracy levels are maintained irrespective of the underlying grid structure. Besides that, it is also required that the volume average (2) of the reconstruction polynomial (5) is satisfied on a compact neighborhood of elements around Ω_α [20]. The latter is also referred to as the k-exact conservation of the mean [21,22]. These tasks are typically approached by solving a least-squares problem for the unknown polynomial coefficients using the known volume averages from the kth neighborhood $\{\beta_\alpha^{(k)}\}$ [20,21,23]. However, for unstructured grids, this method leads to complex data structures and hence to a high implementation effort if it is to be integrated into established flow solvers at a later stage. This problem is avoided in the k-exact multiple-correction approach [10,12], where the unknown polynomial coefficients $(\phi|_{\boldsymbol{x}_\alpha}^{(k+1)}, \partial\phi/\partial x_i|_{\boldsymbol{x}_\alpha}^{(k)}, \partial^2\phi/(\partial x_i \partial x_j)|_{\boldsymbol{x}_\alpha}^{(k-1)}, \ldots)$ are estimated via successive correction steps that rely on a routine, which is often used in state-of-the-art finite-volume solvers: the Green–Gauss gradient algorithm. In the scope of median-dual grids, the latter approximates the gradient of ϕ at location $\boldsymbol{x}_\alpha$ from the known volume averages of all direct neighbors of Ω_α via

$$\frac{\partial \phi}{\partial x_i}\Big|_{\boldsymbol{x}_\alpha}^{(0)} = \frac{1}{|\Omega_\alpha|} \sum_{\beta \in \{\beta_\alpha^{(1)}\}} \frac{1}{2}\left(\overline{\phi}_\alpha + \overline{\phi}_\beta\right) \mathcal{S}_i^{(\alpha\beta)} \tag{6}$$

where $\mathcal{S}_i^{(\alpha\beta)}$ depicts the surface normal vector between two adjacent elements Ω_α and Ω_β. Given these gradient approximations, one can construct further derivatives by applying the same method again and again, for example, for the Hessian matrix of ϕ:

$$\frac{\partial^2 \phi}{\partial x_i \partial x_j}\Big|_{\boldsymbol{x}_\alpha}^{(0)} = \frac{1}{|\Omega_\alpha|} \sum_{\beta \in \{\beta_\alpha^{(1)}\}} \frac{1}{2}\left(\frac{\partial \phi}{\partial x_i}\Big|_{\boldsymbol{x}_\alpha}^{(0)} + \frac{\partial \phi}{\partial x_i}\Big|_{\boldsymbol{x}_\beta}^{(0)}\right) \mathcal{S}_j^{(\alpha\beta)} \tag{7}$$

Apart from Cartesian grids, these calculated derivative operators are not suitable to be used as coefficients for the reconstruction polynomial (5), because they do not fulfill the required spatial accuracy properties (as indicated by the superscripts). The idea of the multi-correction approach is to circumvent these accuracy limitations by multiplying the approximate Green–Gaussian derivatives with grid-specific correction matrices $\boldsymbol{G}_\alpha^{(k)}$. For a one-exact gradient, this correction step looks as follows:

$$\frac{\partial \phi}{\partial x_i}\Big|_{\boldsymbol{x}_\alpha}^{(1)} = G_{\alpha,ij}^{(1)} \frac{\partial \phi}{\partial x_j}\Big|_{\boldsymbol{x}_\alpha}^{(0)} \tag{8}$$

This gradient can be used in a subsequent step to calculate the next derivative, which in turn is used for a further gradient correction:

$$\frac{\partial^2 \phi}{\partial x_i \partial x_j}\Big|_{\boldsymbol{x}_\alpha}^{(1)} = H_{\alpha,ijkl}^{(1)} \frac{\partial^2 \phi}{\partial x_k \partial x_l}\Big|_{\boldsymbol{x}_\alpha}^{(0)} \tag{9a}$$

$$\frac{\partial \phi}{\partial x_i}\Big|_{\boldsymbol{x}_\alpha}^{(2)} = \frac{\partial \phi}{\partial x_i}\Big|_{\boldsymbol{x}_\alpha}^{(1)} - G_{\alpha,ijk}^{(2)} \frac{\partial^2 \phi}{\partial x_j \partial x_k}\Big|_{\boldsymbol{x}_\alpha}^{(1)} \tag{9b}$$

where $\boldsymbol{H}_\alpha^{(1)}$ and $\boldsymbol{G}_\alpha^{(2)}$ denote further correction matrices required for a two-exact reconstruction. In this way, derivatives can be successively constructed with higher levels of accuracy and in turn be used as coefficients in the reconstruction polynomial (5). The data for enhancing the order of accuracy are implicitly transferred through derivatives of adjacent elements. This is a major advantage, as no complex MPI exchange of element stencils across boundaries of decomposed domains is required, which considerably simplifies the implementation of the method in terms of parallelization efficiency toward nonlocal k-exact finite-volume schemes. The effect of the different correction steps is highlighted in Fig. 2, where a grid convergence study is performed for the numerical gradient of an example function $\phi(\boldsymbol{x})$:

$$\phi(\boldsymbol{x}) = A\sin(2\pi f x_1 x_2)\exp\left(-\frac{x_1^2+x_2^2}{\sigma^2}\right) \tag{10}$$

with $A = 50$, $f = 2/L^2$, $\sigma = L/10$, and $L = 1$ m. The gradients are calculated on a quadratic computational domain $\Omega \in [-L/2, L/2]\times[-L/2, L/2]$ which is discretized by distorted triangular elements, as depicted on the right of Fig. 2 and where the mean grid width $h = L/\sqrt{N}$ is reduced successively. The results are assessed through the L^2-norm error E_{L^2}. The exactness of the gradient and thus the number of correction steps is denoted by k. Accordingly, $k = 0$ denotes the Green–Gauss gradient (6), which runs into a constant error level due to the strong element distortion. The two-exact gradient from Eq. (9), on the other hand, exhibits a spatial accuracy of $\mathcal{O}(h^2)$ even with severely distorted elements. For $k = 2$, Fig. 2 also shows the L^2-error of the second derivative $\partial^2\phi/\partial x_1\partial x_2$ in the form of the dashed line. Its value range is shown on the right-hand abscissa. As a result of the correction step (9a), this derivative preserves a first-order accuracy.

The correction matrices $\boldsymbol{G}_\alpha^{(1)}, \boldsymbol{G}_\alpha^{(2)}, \boldsymbol{H}_\alpha^{(1)}$ represent tensors of different ranks, whose calculation for cell-centered grids can be found in the work of Pont et al. [10] and for median-dual grids in our previous work [12]. There, it is also shown how the costly tensor product in Eq. (9a) can be turned to a matrix-vector product by using the symmetry properties of the Hessian. The calculation of all correction matrices depends primarily on grid-dependent metrics, which are referred to as geometric volume moments. These are generally defined by

$$\mathcal{M}_{i_1 i_2 \dots i_p,\alpha} = \frac{1}{|\Omega_\alpha|}\iiint_{\Omega_\alpha}\left(x_{i_1}-x_{i_1,\alpha}\right)\left(x_{i_2}-x_{i_2,\alpha}\right)\dots\left(x_{i_p}-x_{i_p,\alpha}\right)\mathrm{d}V \tag{11}$$

where $\mathcal{M}_{i_1 i_2 \dots i_p,\alpha}$ refers to a moment of rank p. It remains to calculate the point value of the solution at the primary grid node $\phi|_{\boldsymbol{x}_\alpha}^{(k+1)}$, which represents a coefficient to be determined in the reconstruction polynomial given in Eq. (5). A volumetric averaging of Eq. (5) shows that this can be achieved using the volume average $\overline{\phi}_\alpha$, the introduced geometric moments $\mathcal{M}_{i_1 i_2 \dots i_p,\alpha}$, and the respective corrected derivatives:

$$\phi|_{\boldsymbol{x}_\alpha}^{(k+1)} = \overline{\phi}_\alpha - \left.\frac{\partial\phi}{\partial x_{i_1}}\right|_{\boldsymbol{x}_\alpha}^{(k)}\mathcal{M}_{i_1,\alpha} - \dots - \frac{1}{k!}\left.\frac{\partial^k\phi}{\partial x_{i_1}\dots\partial x_{i_k}}\right|_{\boldsymbol{x}_\alpha}^{(1)}\mathcal{M}_{i_1\dots i_k,\alpha} + \mathcal{O}\left(h^{k+1}\right) \tag{12}$$

Once the reconstruction polynomials are calculated, they are used to approximate the surface integrals of transport equation (1) to close the system of equations. In this work, the approximation of the numerical fluxes $F_C^{(\alpha\beta)}$ and $F_D^{(\alpha\beta)}$ is realized with a single-point integration, which is based on a Taylor series expansion around a point $\boldsymbol{x}_\Gamma = (\boldsymbol{x}_\alpha + \boldsymbol{x}_\beta)/2$ located on the surface $A_{\alpha\beta}$:

$$\iint_{A_{\alpha\beta}} f_i n_i\,\mathrm{d}A = f_i|_{\boldsymbol{x}_\Gamma}\mathcal{S}_i^{(\alpha\beta)} + \left.\frac{\partial f_i}{\partial x_{j_1}}\right|_{\boldsymbol{x}_\Gamma}\mathcal{S}_{i,j_1}^{(\alpha\beta,\Gamma)} + \dots + \frac{1}{k!}\left.\frac{\partial^k f_i}{\partial x_{j_1}\dots\partial x_{j_k}}\right|_{\boldsymbol{x}_\Gamma}\mathcal{S}_{i,j_1\dots j_k}^{(\alpha\beta,\Gamma)} + \mathcal{O}\left(h^{k+1}\right) \tag{13}$$

In this way, any flux function f_i can be integrated by means of the reconstructed point value $\phi|_{\boldsymbol{x}_\Gamma}$ and its derivatives at $\boldsymbol{x}_\Gamma$, as long as these point values maintain appropriate orders of accuracies. The integration method is based on the introduction of rank p geometric surface moments, which ensure a proper integration of the surface-integral in a single point, regardless of the shape of the surface $A_{\alpha\beta}$. They are generally defined as

$$\mathcal{S}_{i,j_1 j_2\dots j_p}^{(\alpha\beta,\Gamma)} = \iint_{A_{\alpha\beta}} n_i\left(x_{j_1}-x_{j_1,\Gamma}\right)\left(x_{j_2}-x_{j_2,\Gamma}\right)\dots\left(x_{j_p}-x_{j_p,\Gamma}\right)\mathrm{d}A \tag{14}$$

where the subscripts i and j_p are separated by a comma to highlight that i indicates the face normal direction and j_p the spatial direction of the terms $(x_{j_p} - x_{j_p,\Gamma})$. The superscripts $(\alpha\beta,\Gamma)$ indicate the elements Ω_α and Ω_β adjacent to the face, as well as the point $\boldsymbol{x}_\Gamma$ where the Taylor series expansion is located. The rank zero surface moment $\mathcal{S}_i^{(\alpha\beta)}$ does not include the superscript Γ because it only refers to the joint normal of the face $A_{\alpha\beta}$ and is thus independent of $\boldsymbol{x}_\Gamma$. The same surface moment definition also holds for faces $A_{\alpha\delta}$ located at domain boundaries.

The approximation of convective fluxes $f_i = u_i\phi$ is based on a novel central discretization approach with an adaptive numerical dissipation control. It ensures the stability of the scheme while the numerical dissipation is reduced to a minimum. This greatly enhances the simulation results compared to conventional discretization schemes for convective fluxes, regardless of empirical flow parameters. The fluxes can be calculated with a one- and two-exact reconstruction and thus achieve a second and third spatial order of accuracy, respectively. The approach has been described in detail in our recent work [13].

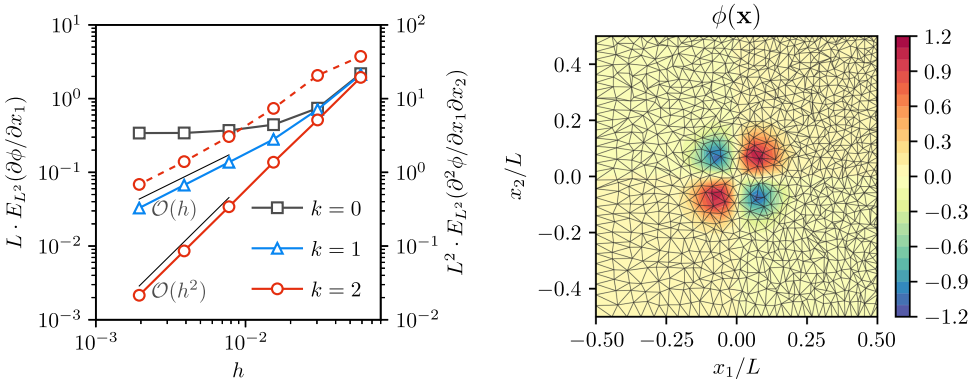

Fig. 2 Convergence study for the gradient of Eq. (10), calculated on distorted triangular grids as shown on the right. Solid lines indicate the errors for the gradient, and the dashed red line refers to the error of the second derivative $\partial^2\phi/\partial x_1\partial x_2$ (only calculated for $k = 2$).

A. Viscous Fluxes at Interior Faces

The following derivations are presented for a two-exact reconstruction. The starting point for the calculation of viscous fluxes at interior faces is the insertion of the flux function $f_i = D(\partial\phi/\partial x_i)$ into Eq. (13), which gives

$$F_D^{(\alpha\beta)} = D\left.\frac{\partial\phi}{\partial x_i}\right|_{\boldsymbol{x}_\Gamma} \mathcal{S}_i^{(\alpha\beta)} + D\left.\frac{\partial^2\phi}{\partial x_i \partial x_j}\right|_{\boldsymbol{x}_\Gamma} \mathcal{S}_{i,j}^{(\alpha\beta,\Gamma)} + |A_{\alpha\beta}|\mathcal{O}(h^2) \tag{15}$$

We start by expressing the gradient $\partial\phi/\partial x_i|_{\boldsymbol{x}_\Gamma}$ at the surface $A_{\alpha\beta}$ in terms of the reconstruction polynomial of the adjacent elements Ω_α and Ω_β. It is desirable to do this in terms of the volume averages $\overline{\phi}_\alpha$ and $\overline{\phi}_\beta$ to obtain a stronger coupling of the underlying system of equations and a resulting suppression of parasitic errors. This is also the main idea of the discretization scheme by Mathur and Murthy [17], which will be extended for the approximation of Eq. (15) in the context of a k-exact reconstruction. It is also referred to as face-tangent scheme [24–26], which is frequently used to discretize viscous fluxes on unstructured grids [27] and which is based on the works of Muzaferija and Gosman [28] and Demirdžić and Muzaferija [29]. All of these schemes rely on the separation of the scalar product between the gradient and the surface normal $(\partial\phi/\partial x_i|_{\boldsymbol{x}_\Gamma})\mathcal{S}_i^{(\alpha\beta)}$ into an orthogonal and a nonorthogonal part [30]

$$\left.\frac{\partial\phi}{\partial x_i}\right|_{\boldsymbol{x}_\Gamma} \mathcal{S}_i^{(\alpha\beta)} = \underbrace{\varepsilon^{(\alpha\beta)}\left.\frac{\partial\phi}{\partial x_i}\right|_{\boldsymbol{x}_\Gamma} \Delta x_i^{(\alpha\beta)}}_{\text{orthogonal}} + \underbrace{\varepsilon^{(\alpha\beta)}\left.\frac{\partial\phi}{\partial x_i}\right|_{\boldsymbol{x}_\Gamma} \Delta\tilde{x}_i^{(\alpha\beta)}}_{\text{non-orthogonal}} \tag{16}$$

with the distance vectors $\Delta x_i^{(\alpha\beta)} := x_{i,\beta} - x_{i,\alpha}$ and $\Delta\tilde{x}_i^{(\alpha\beta)} := \mathcal{S}_i^{(\alpha\beta)}/\varepsilon^{(\alpha\beta)} - \Delta x_i^{(\alpha\beta)}$. The geometric quantity $\varepsilon^{(\alpha\beta)}$ places a degree of freedom for the construction of the scheme and can be used to unify the mentioned approaches, which is shown in the work of Jasak [30]. For the present work, the parameter is calculated according to the Mathur–Murthy scheme:

$$\varepsilon^{(\alpha\beta)} = \frac{\mathcal{S}_i^{(\alpha\beta)}\mathcal{S}_i^{(\alpha\beta)}}{\Delta x_j^{(\alpha\beta)}\mathcal{S}_j^{(\alpha\beta)}} \tag{17}$$

This formulation is also known as an overrelaxed approach [30] and leads to a stronger weighting of the nonorthogonal part when the surface normal $\mathcal{S}_i^{(\alpha\beta)}$ and the distance vector $\Delta x_i^{(\alpha\beta)}$ are not aligned. This relationship is shown in Fig. 3. The further derivation requires us to introduce the points $\boldsymbol{x}_{\tilde{\alpha}}$ and $\boldsymbol{x}_{\tilde{\beta}}$ that are defined by

$$\boldsymbol{x}_{\tilde{\alpha}} = \boldsymbol{x}_\Gamma - \tfrac{1}{2}\Delta\tilde{\boldsymbol{x}}^{(\alpha\beta)}, \qquad \boldsymbol{x}_{\tilde{\beta}} = \boldsymbol{x}_\Gamma + \tfrac{1}{2}\Delta\tilde{\boldsymbol{x}}^{(\alpha\beta)} \tag{18}$$

The factor $1/2$ for the definition of $\boldsymbol{x}_{\tilde{\alpha}}$ and $\boldsymbol{x}_{\tilde{\beta}}$ is chosen to simplify the derivation. However, it can be shown that the actual choice of this factor does not influence the final outcome.

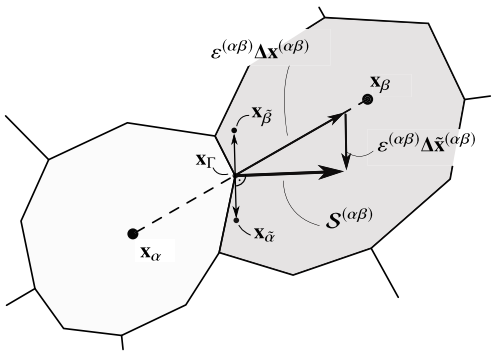

Fig. 3 Splitting of the surface normal $\mathcal{S}^{\alpha\beta}$ into a part $\varepsilon^{(\alpha\beta)}\Delta x^{(\alpha\beta)}$ that is projected onto $\Delta x^{(\alpha\beta)}$ and a part $\varepsilon^{(\alpha\beta)}\Delta\tilde{x}^{(\alpha\beta)}$ orthogonal to it.

Our target is to approximate the scalar products $(\partial\phi/\partial x_i|_{\boldsymbol{x}_\Gamma})\Delta x_i^{(\alpha\beta)}$ and $(\partial\phi/\partial x_i|_{\boldsymbol{x}_\Gamma})\Delta\tilde{x}_i^{(\alpha\beta)}$ in terms of the reconstruction polynomials of the adjacent elements Ω_α and Ω_β. For this, a Taylor series expansion is constructed around point $\boldsymbol{x}_\Gamma = (\boldsymbol{x}_\alpha + \boldsymbol{x}_\beta)/2$, which is located at the face $A_{\alpha\beta}$. For $k = 2$ this leads to the following expression:

$$\phi(\boldsymbol{x}) = \phi|_{\boldsymbol{x}_\Gamma} + \left.\frac{\partial\phi}{\partial x_i}\right|_{\boldsymbol{x}_\Gamma}(x_i - x_{i,\Gamma}) + \frac{1}{2}\left.\frac{\partial^2\phi}{\partial x_i\partial x_j}\right|_{\boldsymbol{x}_\Gamma}(x_i - x_{i,\Gamma})(x_j - x_{j,\Gamma}) + \mathcal{O}(h^3) \tag{19}$$

Equation (19) is used to express the point values of ϕ at the primary grid node locations of both adjacent elements:

$$\phi|_{\boldsymbol{x}_\alpha} = \phi|_{\boldsymbol{x}_\Gamma} - \frac{1}{2}\left.\frac{\partial\phi}{\partial x_i}\right|_{\boldsymbol{x}_\Gamma}\Delta x_i^{(\alpha\beta)} + \frac{1}{8}\left.\frac{\partial^2\phi}{\partial x_i\partial x_j}\right|_{\boldsymbol{x}_\Gamma}\Delta x_i^{(\alpha\beta)}\Delta x_j^{(\alpha\beta)} + \mathcal{O}(h^3) \tag{20a}$$

$$\phi|_{\boldsymbol{x}_\beta} = \phi|_{\boldsymbol{x}_\Gamma} + \frac{1}{2}\left.\frac{\partial\phi}{\partial x_i}\right|_{\boldsymbol{x}_\Gamma}\Delta x_i^{(\alpha\beta)} + \frac{1}{8}\left.\frac{\partial^2\phi}{\partial x_i\partial x_j}\right|_{\boldsymbol{x}_\Gamma}\Delta x_i^{(\alpha\beta)}\Delta x_j^{(\alpha\beta)} + \mathcal{O}(h^3) \tag{20b}$$

Subtracting these two equations from each other finally leads to an expression that allows the orthogonal part of the flux to be approximated by

$$\left.\frac{\partial\phi}{\partial x_i}\right|_{\boldsymbol{x}_\Gamma}\Delta x_i^{(\alpha\beta)} = \phi|_{\boldsymbol{x}_\beta} - \phi|_{\boldsymbol{x}_\alpha} + \mathcal{O}(h^3) \tag{21}$$

To approximate the nonorthogonal term of Eq. (16), we evaluate the Taylor polynomial from Eq. (19) at both points $\boldsymbol{x}_{\tilde{\alpha}}$ and $\boldsymbol{x}_{\tilde{\beta}}$ that have been defined in Eq. (18):

$$\phi|_{\boldsymbol{x}_{\tilde{\alpha}}} = \phi|_{\boldsymbol{x}_\Gamma} - \frac{1}{2}\left.\frac{\partial\phi}{\partial x_i}\right|_{\boldsymbol{x}_\Gamma}\Delta\tilde{x}_i^{(\alpha\beta)} + \frac{1}{8}\left.\frac{\partial^2\phi}{\partial x_i\partial x_j}\right|_{\boldsymbol{x}_\Gamma}\Delta\tilde{x}_i^{(\alpha\beta)}\Delta\tilde{x}_j^{(\alpha\beta)} + \mathcal{O}(h^3) \tag{22a}$$

$$\phi|_{\boldsymbol{x}_{\tilde{\beta}}} = \phi|_{\boldsymbol{x}_\Gamma} + \frac{1}{2}\left.\frac{\partial\phi}{\partial x_i}\right|_{\boldsymbol{x}_\Gamma}\Delta\tilde{x}_i^{(\alpha\beta)} + \frac{1}{8}\left.\frac{\partial^2\phi}{\partial x_i\partial x_j}\right|_{\boldsymbol{x}_\Gamma}\Delta\tilde{x}_i^{(\alpha\beta)}\Delta\tilde{x}_j^{(\alpha\beta)} + \mathcal{O}(h^3) \tag{22b}$$

and solve for the scalar product $\partial\phi/\partial x_i|_{\boldsymbol{x}_\Gamma}\Delta\tilde{x}_i^{(\alpha\beta)}$. This results in the following expression:

$$\left.\frac{\partial\phi}{\partial x_i}\right|_{\boldsymbol{x}_\Gamma}\Delta\tilde{x}_i^{(\alpha\beta)} = \phi|_{\boldsymbol{x}_{\tilde{\beta}}} - \phi|_{\boldsymbol{x}_{\tilde{\alpha}}} + \mathcal{O}(h^3) \tag{23}$$

On fully orthogonal grids, both points $\boldsymbol{x}_{\tilde{\alpha}}$ and $\boldsymbol{x}_{\tilde{\beta}}$ coincide with $\boldsymbol{x}_\Gamma$, which causes this equation to vanish. It remains to approximate the unknown point values of ϕ at $\boldsymbol{x}_{\tilde{\alpha}}$ and $\boldsymbol{x}_{\tilde{\beta}}$ with respective orders of accuracies. This is achieved by evaluating the k-exact reconstruction polynomials from Eq. (5) of both adjacent elements Ω_α and Ω_β at $\boldsymbol{x}_\Gamma$ and by performing a central averaging:

$$\phi(\boldsymbol{x}_{\tilde{\alpha}}) = \frac{1}{2}\left(\phi^{(k+1)}(\boldsymbol{x}_{\tilde{\alpha}};\boldsymbol{x}_\alpha) + \phi^{(k+1)}(\boldsymbol{x}_{\tilde{\alpha}};\boldsymbol{x}_\beta)\right) + \mathcal{O}\left(h^{k+1}\right) \tag{24a}$$

$$\phi(\boldsymbol{x}_{\tilde{\beta}}) = \frac{1}{2}\left(\phi^{(k+1)}(\boldsymbol{x}_{\tilde{\beta}};\boldsymbol{x}_\alpha) + \phi^{(k+1)}(\boldsymbol{x}_{\tilde{\beta}};\boldsymbol{x}_\beta)\right) + \mathcal{O}\left(h^{k+1}\right) \tag{24b}$$

After some rearrangement of terms and under consideration of the definition of $\boldsymbol{x}_{\tilde{\alpha}}$ and $\boldsymbol{x}_{\tilde{\beta}}$, we obtain the following formulation for the nonorthogonal part:

$$\left.\frac{\partial\phi}{\partial x_i}\right|_{\boldsymbol{x}_\Gamma}\Delta\tilde{x}_i^{(\alpha\beta)} = \frac{1}{2}\left(\left.\frac{\partial\phi}{\partial x_i}\right|_{\boldsymbol{x}_\alpha} + \left.\frac{\partial\phi}{\partial x_i}\right|_{\boldsymbol{x}_\beta}\right)\Delta\tilde{x}_i^{(\alpha\beta)} - \frac{1}{4}\left(\left.\frac{\partial^2\phi}{\partial x_i\partial x_j}\right|_{\boldsymbol{x}_\beta} - \left.\frac{\partial^2\phi}{\partial x_i\partial x_j}\right|_{\boldsymbol{x}_\alpha}\right)\Delta\tilde{x}_i^{(\alpha\beta)}\Delta x_j^{(\alpha\beta)} + \mathcal{O}(h^3) \tag{25}$$

Inserting both relations for $(\partial\phi/\partial x_i)|_{\boldsymbol{x}_\Gamma}\Delta x_i^{(\alpha\beta)}$ and $(\partial\phi/\partial x_i)|_{\boldsymbol{x}_\Gamma}\Delta\tilde{x}_i^{(\alpha\beta)}$ into Eq. (16) and using the relation $\varepsilon^{(\alpha\beta)}\Delta\tilde{x}_i^{(\alpha\beta)} = \mathcal{S}_i^{(\alpha\beta)} - \varepsilon^{(\alpha\beta)}\Delta x_i^{(\alpha\beta)}$ yields the following expression for the viscous fluxes:

$$\left.\frac{\partial\phi}{\partial x_i}\right|_{\boldsymbol{x}_\Gamma}\mathcal{S}_i^{(\alpha\beta)} = \underbrace{\varepsilon^{(\alpha\beta)}(\phi|_{\boldsymbol{x}_\beta} - \phi|_{\boldsymbol{x}_\alpha}) + \frac{1}{2}\left(\left.\frac{\partial\phi}{\partial x_i}\right|_{\boldsymbol{x}_\alpha} + \left.\frac{\partial\phi}{\partial x_i}\right|_{\boldsymbol{x}_\beta}\right)\left(\mathcal{S}_i^{(\alpha\beta)} - \varepsilon^{(\alpha\beta)}\Delta x_i^{(\alpha\beta)}\right)}_{\text{Mathur-Murthyscheme}} - \frac{1}{4}\left(\left.\frac{\partial^2\phi}{\partial x_i\partial x_j}\right|_{\boldsymbol{x}_\beta} - \left.\frac{\partial^2\phi}{\partial x_i\partial x_j}\right|_{\boldsymbol{x}_\alpha}\right)\left(\mathcal{S}_i^{(\alpha\beta)} - \varepsilon^{(\alpha\beta)}\Delta x_i^{(\alpha\beta)}\right)\Delta x_j^{(\alpha\beta)} + \mathcal{O}(h^3) \tag{26}$$

This expression calculates the scalar product $(\partial\phi/\partial x_i|_{\boldsymbol{x}_\Gamma})\mathcal{S}_i^{(\alpha\beta)}$ with a third-order accuracy in space when the various derivatives and point values are approximated with corresponding accuracy levels. The latter is given for the case of a two-exact reconstruction, where the derivatives are replaced by their numerical counterparts from Eq. (9) and where point values are approximated using Eq. (12). For $k < 2$, the second term in Eq. (26) is omitted, and for $k = 0$ the scheme reduces to the original scheme by Mathur and Murthy [17], where the point values of the first term are replaced by volumetric averages.

After some rearrangement of terms and by introducing a variable discretization coefficient a, Eq. (26) can be converted into the well-known α-damping scheme by Nishikawa [16], which mimics the form of the Rusanov flux [16]

$$\left.\frac{\partial\phi}{\partial x_i}\right|_{\boldsymbol{x}_\Gamma}\mathcal{S}_i^{(\alpha\beta)} = \frac{1}{2}\left(\left.\frac{\partial\phi}{\partial x_i}\right|_{\boldsymbol{x}_L} + \left.\frac{\partial\phi}{\partial x_i}\right|_{\boldsymbol{x}_R}\right)\mathcal{S}_i^{(\alpha\beta)} + a\varepsilon^{(\alpha\beta)}\left(\phi|_{\boldsymbol{x}_R} - \phi|_{\boldsymbol{x}_L}\right) \tag{27}$$

In Nishikawa's work, this equation is obtained from a first-order hyperbolic relaxation system for diffusion that is discretized by an upwind advection scheme. The dissipation term of the advection scheme manifests itself in a high-frequency damping term on the right, which scales with the coefficient a (which is designated by α in Nishikawa's work). The latter can be adjusted to enhance the order of accuracy on Cartesian grids. The first term is called the consistent term and is used to approximate the physical flux [16]. Both terms are calculated from reconstructed solutions from the left and the right element (which here denote the elements Ω_α and Ω_β, respectively). In Nishikawa's work, these values are based on a linear reconstruction, which is analogous to a one-exact reconstruction in this work. He also showed that choosing the coefficient a to a value of $4/3$ results in a fourth-order accurate discretization of the viscous operator on Cartesian grids. Note that the geometric quantity $\varepsilon^{(\alpha\beta)} = |A_{\alpha\beta}|/(2\sqrt{T_r D})$ can be related to a relaxation time T_r, which was introduced by Nishikawa to express the diffusion equation in terms of a first-order hyperbolic relaxation system, with $|A_{\alpha\beta}|$ being the magnitude of the surface normal vector. If a two-exact reconstruction is considered, the face derivatives are calculated by

$$\left.\frac{\partial\phi}{\partial x_i}\right|_{\boldsymbol{x}_L} = \left.\frac{\partial\phi}{\partial x_i}\right|_{\boldsymbol{x}_\alpha} + \frac{1}{2}\left.\frac{\partial^2\phi}{\partial x_i\partial x_j}\right|_{\boldsymbol{x}_\alpha}\Delta x_j^{(\alpha\beta)}, \qquad \left.\frac{\partial\phi}{\partial x_i}\right|_{\boldsymbol{x}_R} = \left.\frac{\partial\phi}{\partial x_i}\right|_{\boldsymbol{x}_\beta} - \frac{1}{2}\left.\frac{\partial^2\phi}{\partial x_i\partial x_j}\right|_{\boldsymbol{x}_\beta}\Delta x_j^{(\alpha\beta)} \tag{28}$$

and the reconstructed values of ϕ from both sides are approximated by

$$\phi|_{\boldsymbol{x}_L} = \phi|_{\boldsymbol{x}_\alpha} + \frac{1}{2}\left.\frac{\partial\phi}{\partial x_i}\right|_{\boldsymbol{x}_\alpha}\Delta x_i^{(\alpha\beta)} + \frac{c}{4}\left.\frac{\partial^2\phi}{\partial x_i\partial x_j}\right|_{\boldsymbol{x}_\alpha}\Delta x_i^{(\alpha\beta)}\Delta x_j^{(\alpha\beta)}, \qquad \phi|_{\boldsymbol{x}_R} = \phi|_{\boldsymbol{x}_\beta} - \frac{1}{2}\left.\frac{\partial\phi}{\partial x_i}\right|_{\boldsymbol{x}_\beta}\Delta x_i^{(\alpha\beta)} + \frac{c}{4}\left.\frac{\partial^2\phi}{\partial x_i\partial x_j}\right|_{\boldsymbol{x}_\beta}\Delta x_i^{(\alpha\beta)}\Delta x_j^{(\alpha\beta)} \tag{29}$$

where the point values $\phi|_{\boldsymbol{x}_\alpha}$ and $\phi|_{\boldsymbol{x}_\beta}$ are given by

$$\phi|_{\boldsymbol{x}_\alpha} = \overline{\phi}_\alpha - b\left(\left.\frac{\partial\phi}{\partial x_i}\right|_{\boldsymbol{x}_\alpha}\mathcal{M}_{i,\alpha} + \frac{1}{2}\left.\frac{\partial^2\phi}{\partial x_i\partial x_j}\right|_{\boldsymbol{x}_\alpha}\mathcal{M}_{ij,\alpha}\right), \qquad \phi|_{\boldsymbol{x}_\beta} = \overline{\phi}_\beta - b\left(\left.\frac{\partial\phi}{\partial x_i}\right|_{\boldsymbol{x}_\beta}\mathcal{M}_{i,\beta} + \frac{1}{2}\left.\frac{\partial^2\phi}{\partial x_i\partial x_j}\right|_{\boldsymbol{x}_\beta}\mathcal{M}_{ij,\beta}\right) \tag{30}$$

Here we introduced the additional coefficients b and c, such that Eq. (26) is recovered for a choice of $a = b = c = 1$. This formulation is very similar to the method presented in the work of Chamarthi et al. [14,15] for a finite difference method, which was used to extend Nishikawa's α-damping scheme to a sixth order of accuracy. In fact, it will be shown that a dedicated choice of all three parameters can also yield a sixth-order scheme on Cartesian grids. Note that with the chosen definition of c, the Hessian terms in Eq. (29) scale with a factor of $1/4$, although a straightforward extension of Nishikawa's α-damping scheme with a two-exact reconstruction would result in the value $1/8$, similar to the Hessian terms in Eq. (20). Under consideration of the coefficients a, b, and c, Eq. (26) can finally be written in terms of

$$\left.\frac{\partial\phi}{\partial x_i}\right|_{\boldsymbol{x}_\Gamma}\mathcal{S}_i^{(\alpha\beta)} = a\varepsilon^{(\alpha\beta)}(\phi|_{\boldsymbol{x}_\beta} - \phi|_{\boldsymbol{x}_\alpha}) + \frac{1}{2}\left(\left.\frac{\partial\phi}{\partial x_i}\right|_{\boldsymbol{x}_\alpha} + \left.\frac{\partial\phi}{\partial x_i}\right|_{\boldsymbol{x}_\beta}\right)\left(\mathcal{S}_i^{(\alpha\beta)} - a\varepsilon^{(\alpha\beta)}\Delta x_i^{(\alpha\beta)}\right) - \frac{1}{4}\left(\left.\frac{\partial^2\phi}{\partial x_i\partial x_j}\right|_{\boldsymbol{x}_\beta} - \left.\frac{\partial^2\phi}{\partial x_i\partial x_j}\right|_{\boldsymbol{x}_\alpha}\right)\left(\mathcal{S}_i^{(\alpha\beta)} - ac\varepsilon^{(\alpha\beta)}\Delta x_i^{(\alpha\beta)}\right)\Delta x_j^{(\alpha\beta)} + \mathcal{O}(h^3) \tag{31}$$

where coefficient b is used in the point value approximation according to Eq. (30). The comparison reveals that the high-frequency damping controlled by the jump of the solution at the interface in the α-damping scheme simply corresponds to a scaling of the geometric quantity $\varepsilon^{(\alpha\beta)}$ in the Mathur–Murthy scheme. The latter can be interpreted as an alternative orientation of the nonorthogonal distance vector $\Delta\tilde{x}_i^{(\alpha\beta)}$ and thus a shift of points $\boldsymbol{x}_{\tilde{\alpha}}$ and $\boldsymbol{x}_{\tilde{\beta}}$, such that the second term in Eq. (31) no longer vanishes on Cartesian grids. This shift is depicted exemplarily in Fig. 4 for the cases $a = 1$ and $a = 4/3$. A similar effect is achieved via coefficient c for the two-exact correction term. On the other hand, coefficient b only affects the calculation of the point values $\phi|_{\boldsymbol{x}_\alpha}$ and $\phi|_{\boldsymbol{x}_\beta}$ in Eq. (30).

The insight of the former comparison to the α-damping scheme can be used to fine-tune the coefficients a, b, and c for higher orders of accuracy on Cartesian grids. For this purpose, a one-dimensional diffusion equation $\partial\phi/\partial t = D\partial^2\phi/\partial x_1^2$ is discretized via Eq. (31) on a periodic domain $\Omega \in [0, L]$. The latter consists of N elements Ω_α of length h, whose centroids $x_{1,\alpha}$ are placed equidistantly. Inserting a smooth function into the scheme and expanding it reveals the numerical truncation error $\mathcal{E}$:

$$\int_{\Omega_\alpha}\frac{\partial^2\phi}{\partial x_1^2}\,\mathrm{d}x_1 = \left(\left.\frac{\partial\phi}{\partial x_1}\right|_{\boldsymbol{x}_{\alpha+1/2}} - \left.\frac{\partial\phi}{\partial x_1}\right|_{\boldsymbol{x}_{\alpha-1/2}}\right) + \mathcal{E}(\phi, h) \tag{32}$$

where $\boldsymbol{x}_{\alpha-1/2}$ and $\boldsymbol{x}_{\alpha+1/2}$ correspond to the locations of the left and right faces of Ω_α. In the case of a one-exact reconstruction, where second derivatives are equal to zero, the truncation error simplifies to

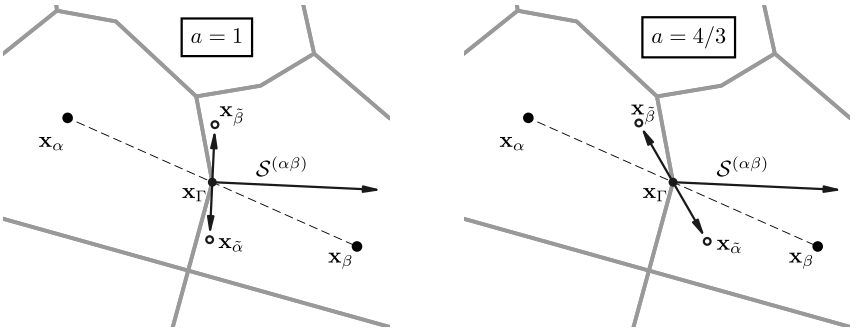

Fig. 4 Influence of the discretization parameter a on the location of the points $x_{\tilde{\alpha}}$ and $x_{\tilde{\beta}}$.

$$\mathcal{E}(\phi, h) = \underbrace{\left(\frac{3a-4}{12}\right) h^2 \left.\frac{\partial^4 \phi}{\partial x_1^4}\right|_{\mathbf{x}_\alpha}}_{\mathcal{O}(h^2)} + \mathcal{O}(h^4) \tag{33}$$

Hence, a value of $a = 4/3$ results in a fourth-order accurate scheme, similarly to Nishikawa's α-damping approach [16]. For a two-exact reconstruction, $\mathcal{E}$ is given by

$$\begin{aligned}\mathcal{E}(\phi, h) = &\underbrace{\left(\frac{ab - 6ac + 6a - 2}{24}\right) h^2 \left.\frac{\partial^4 \phi}{\partial x_1^4}\right|_{\mathbf{x}_\alpha}}_{\mathcal{O}(h^2)} \\ &+ \underbrace{\left(\frac{55ab - 330ac + 150a + 162}{2880}\right) h^4 \left.\frac{\partial^6 \phi}{\partial x_1^6}\right|_{\mathbf{x}_\alpha}}_{\mathcal{O}(h^4)} + \mathcal{O}(h^6)\end{aligned} \tag{34}$$

Setting the coefficients to $a = 68/45$, $b = 0$, and $c = 53/68$ results in a sixth-order accurate discretization of the viscous operator. This choice also recovers the sixth-order finite-difference scheme that has been given in the work of Chamarthi et al. [14]. The analysis also shows that our original scheme, which corresponds to $a = b = c = 1$, is accompanied by a second-order accuracy for both $k = 1$ and $k = 2$. Various combinations of coefficients are shown in Table 1, which will be considered in the course of this paper.

The spectral properties of the proposed scheme can be evaluated with a Fourier analysis. Here, the scalar $\overline{\phi}_\alpha$ is decomposed into its Fourier modes $\hat{\phi}_j(t)\exp(I\omega_j\alpha)$, with the scaled wavenumber $\omega_j = 2\pi jh/L$ and the imaginary number $I = \sqrt{-1}$. Insertion of these Fourier modes into the discretized viscous operator reveals the spectral properties by comparison with its Fourier coefficients $\partial^2\phi_j/\partial x^2 = \lambda(\omega_j)\hat{\phi}_j/h^2$ to its analytical counterpart $\partial^2\phi_j/\partial x^2 = -\omega_j^2\hat{\phi}_j/h^2$. The respective curves for the damping factor $\lambda(\omega_j)$ are shown in Fig. 5, where parameters a, b, and c have been chosen according to Table 1. For $k = 1$, $\lambda(\omega_j)$ is calculated according to

$$\lambda(\omega_j) \quad = (a-1)\sin^2(\omega_j) + 2a\big[\cos(\omega_j) - 1\big] \tag{35}$$

Table 1 Considered combinations of the discretization coefficients a, b, c and corresponding labeling of the schemes

Scheme	Exactness k	Truncation error	a	b	c
MM	— —	$\mathcal{O}(h^2)$	1	0	0
*EX*1-2	1	$\mathcal{O}(h^2)$	1	1	— —
*EX*1-4	1	$\mathcal{O}(h^4)$	$\frac{4}{3}$	0	— —
*EX*2-2	2	$\mathcal{O}(h^2)$	1	1	1
*EX*2-6	2	$\mathcal{O}(h^6)$	$\frac{68}{45}$	0	$\frac{53}{68}$

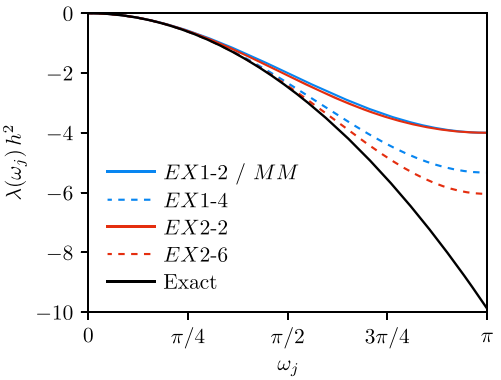

Fig. 5 Damping factor $\lambda(\omega_j)$ for the considered discretization schemes given in Table 1.

The latter reduces to $\lambda(\omega_j) = 2(\cos(\omega_j) - 1)$ for $a = 1$ and thus features similar spectral properties to a typical three-point finite-difference scheme for the viscous operator [16]. In case of $k = 2$, the damping factor $\lambda(\omega_j)$ is given by

$$\begin{aligned}\lambda(\omega_j) = &-\left(\frac{ab}{12} - \frac{ac}{2} - a + \frac{3}{2}\right)\sin^2(\omega_j) \\ &+ \left(\frac{ab}{48} - \frac{ac}{8} + 2a + \frac{1}{8}\right)\cos(\omega_j) \\ &- \left(\frac{ab}{48} - \frac{ac}{8} + \frac{1}{8}\right)\cos(3\omega_j) - 2a\end{aligned} \tag{36}$$

Figure 5 shows that the choice $a = b = c = 1$ resembles similar spectral properties to the one-exact scheme and thus the three-point stencil scheme. In contrast, the damping properties in the high-frequency range are improved for the modified coefficients. Nevertheless, all schemes feature favorable damping properties of high frequencies, which is necessary to suppress odd–even decoupling.

To calculate the final viscous flux in Eq. (15), it remains to determine the second term $\partial^2\phi/(\partial x_i \partial x_j)|_{x_\Gamma}\mathcal{S}_{i,j}^{(\alpha\beta,\Gamma)}$. This term is used to reduce the spatial error for the approximation of the flux integral, as shown in Eq. (13). It does not apply to Cartesian grids, where the geometric surface moments $\mathcal{S}_{i,j}^{(\alpha\beta,\Gamma)}$ reduce to zero. For this reason, it was also not taken into account in the previous error analysis. For a two-exact reconstruction, it is calculated by a central averaging of the two adjacent Hessian matrix entries:

$$\left.\frac{\partial^2\phi}{\partial x_i \partial x_j}\right|_{\mathbf{x}_\Gamma} \mathcal{S}_{i,j}^{(\alpha\beta,\Gamma)} = \frac{1}{2}\left(\left.\frac{\partial^2\phi}{\partial x_i \partial x_j}\right|_{\mathbf{x}_\alpha} + \left.\frac{\partial^2\phi}{\partial x_i \partial x_j}\right|_{\mathbf{x}_\beta}\right)\mathcal{S}_{i,j}^{(\alpha\beta,\Gamma)} + |A_{\alpha\beta}|\mathcal{O}(h^2) \tag{37}$$

The term is not calculated for $k < 2$ because the corresponding reconstruction polynomials inherently lack in their polynomial degree to approximate the required second derivatives.

B. Viscous Fluxes at Dirichlet Boundaries

In the following, the discretization approach for viscous fluxes given previously will be extended for element faces located at Dirichlet boundaries of the computational domain. An extension to Neumann boundary conditions is straightforward, because the respective fluxes can be directly inserted into Eq. (15). However, if Dirichlet boundary conditions are used, the derivative at the surface must be approximated from the imposed boundary values. To maintain the k-exact conservation of the mean, this requires a similar correction as for the interior fluxes. The starting point is the viscous flux of the scalar ϕ over the boundary face $A_{\alpha\delta}$, which is discretized by

$$F_D^{(\alpha\delta)} = D\left.\frac{\partial\phi}{\partial x_i}\right|_{\boldsymbol{x}_\delta}\mathcal{S}_i^{(\alpha\delta)} + |A_{\alpha\beta}|\mathcal{O}(h) \tag{38}$$

In contrast to the internal fluxes, we omit rank one surface moments $\mathcal{S}_{i,j}^{(\alpha\delta,\delta)}$ for the surface integration, because they exhibit much smaller values than interior moments $\mathcal{S}_{i,j}^{(\alpha\beta,\Gamma)}$. The justification for this negligence will also become evident from the results in Sec. IV. In analogy to Eq. (16), the flux is separated into orthogonal and nonorthogonal parts:

$$\left.\frac{\partial\phi}{\partial x_i}\right|_{\boldsymbol{x}_\delta}\mathcal{S}_i^{(\alpha\delta)} = \varepsilon^{(\alpha\delta)}\left.\frac{\partial\phi}{\partial x_i}\right|_{\boldsymbol{x}_\delta}\Delta x_i^{(\alpha\delta)} + \varepsilon^{(\alpha\delta)}\left.\frac{\partial\phi}{\partial x_i}\right|_{\boldsymbol{x}_\delta}\Delta\tilde{x}_i^{(\alpha\delta)} \tag{39}$$

where we introduce the distance vectors $\Delta x_i^{(\alpha\delta)} = x_{i,\delta} - x_{i,\alpha}$ and $\Delta\tilde{x}_i^{(\alpha\delta)} = \mathcal{S}_i^{(\alpha\delta)}/\varepsilon^{(\alpha\delta)} - \Delta x_i^{(\alpha\delta)}$. The parameter $\varepsilon^{(\alpha\delta)}$ is calculated in a similar fashion as for the interior fluxes given in Eq. (17). The orthogonal part requires the product $\partial\phi/\partial x_i|_{\boldsymbol{x}_\delta}\Delta x_i^{(\alpha\delta)}$ to be approximated. For $k = 2$, this is achieved with a Taylor series expansion around the point $\boldsymbol{x}_\delta$ which is located on the surface $A_{\alpha\delta}$. The resulting polynomial is used to approximate the point value $\phi|_{\boldsymbol{x}_\alpha}$ at the primary grid node $\boldsymbol{x}_\alpha$ of the boundary element:

$$\phi|_{\boldsymbol{x}_\alpha} = \phi|_{\boldsymbol{x}_\delta} - \left.\frac{\partial\phi}{\partial x_i}\right|_{\boldsymbol{x}_\delta}\Delta x_i^{(\alpha\delta)} + \frac{1}{2}\left.\frac{\partial^2\phi}{\partial x_i\partial x_j}\right|_{\boldsymbol{x}_\delta}\Delta x_i^{(\alpha\delta)}\Delta x_j^{(\alpha\delta)} + \mathcal{O}(h^3) \tag{40}$$

Substituting the Hessian matrix at point $\boldsymbol{x}_\delta$ via the relation $\partial^2\phi/(\partial x_i\partial x_j)|_{x_\delta} = \partial^2\phi/(\partial x_i\partial x_j)|_{x_\alpha} + \mathcal{O}(h)$ leads to the following expression for the orthogonal part:

$$\left.\frac{\partial\phi}{\partial x_i}\right|_{\boldsymbol{x}_\delta}\Delta x_i^{(\alpha\delta)} = \phi|_{\boldsymbol{x}_\delta} - \phi|_{\boldsymbol{x}_\alpha} + \frac{1}{2}\left.\frac{\partial^2\phi}{\partial x_i\partial x_j}\right|_{\boldsymbol{x}_\alpha}\Delta x_i^{(\alpha\delta)}\Delta x_j^{(\alpha\delta)} + \mathcal{O}(h^3) \tag{41}$$

To compute the nonorthogonal part $(\partial\phi/\partial x_i|_{\boldsymbol{x}_\delta})\Delta\tilde{x}_i^{(\alpha\delta)}$ in Eq. (39), we extrapolate the gradient at surface $A_{\alpha\delta}$ from the interior of element Ω_α and multiply it with the orthogonal distance vector $\Delta\tilde{x}_i^{(\alpha\delta)}$:

$$\left.\frac{\partial\phi}{\partial x_i}\right|_{\boldsymbol{x}_\delta}\Delta\tilde{x}_i^{(\alpha\delta)} = \left(\left.\frac{\partial\phi}{\partial x_i}\right|_{\boldsymbol{x}_\alpha} + \left.\frac{\partial^2\phi}{\partial x_i\partial x_j}\right|_{\boldsymbol{x}_\alpha}\Delta x_j^{(\alpha\delta)}\right)\Delta\tilde{x}_i^{(\alpha\delta)} + \mathcal{O}(h^2) \tag{42}$$

Finally, inserting Eqs. (41) and (42) into Eq. (39) gives the following expression for the scalar product $(\partial\phi/\partial x_i|_{\boldsymbol{x}_\delta})\mathcal{S}_i^{(\alpha\delta)}$:

$$\begin{aligned}\left.\frac{\partial\phi}{\partial x_i}\right|_{\boldsymbol{x}_\delta}\mathcal{S}_i^{(\alpha\delta)} = {}& \varepsilon^{(\alpha\delta)}\left(\phi|_{\boldsymbol{x}_\delta} - \phi|_{\boldsymbol{x}_\alpha} + \frac{1}{2}\left.\frac{\partial^2\phi}{\partial x_i\partial x_j}\right|_{\boldsymbol{x}_\alpha}\Delta x_i^{(\alpha\delta)}\Delta x_j^{(\alpha\delta)}\right)\\ &+ \left.\frac{\partial\phi}{\partial x_i}\right|_{\boldsymbol{x}_\alpha}\left(\mathcal{S}_i^{(\alpha\delta)} - \varepsilon^{(\alpha\delta)}\Delta x_i^{(\alpha\delta)}\right)\\ &+ \left.\frac{\partial^2\phi}{\partial x_i\partial x_j}\right|_{\boldsymbol{x}_\alpha}\left(\mathcal{S}_i^{(\alpha\delta)} - \varepsilon^{(\alpha\delta)}\Delta x_i^{(\alpha\delta)}\right)\Delta x_j^{(\alpha\delta)} + \mathcal{O}(h^2)\end{aligned} \tag{43}$$

A decomposition of terms shows that this expression can also be represented in the form of the α-damping scheme:

$$\begin{aligned}\left.\frac{\partial\phi}{\partial x_i}\right|_{\boldsymbol{x}_\delta}\mathcal{S}_i^{(\alpha\delta)} = {}& \overbrace{\left(\left.\frac{\partial\phi}{\partial x_i}\right|_{\boldsymbol{x}_\alpha} + \left.\frac{\partial^2\phi}{\partial x_i\partial x_j}\right|_{\boldsymbol{x}_\alpha}\Delta x_j^{(\alpha\delta)}\right)}^{=\frac{1}{2}\left(\left.\frac{\partial\phi}{\partial x_i}\right|_{x_L} + \left.\frac{\partial\phi}{\partial x_i}\right|_{x_R}\right)}\mathcal{S}_i^{(\alpha\delta)}\\ &+ \varepsilon^{(\alpha\delta)}\underbrace{\left(\phi|_{\boldsymbol{x}_\delta} - \phi|_{\boldsymbol{x}_\alpha} - \left.\frac{\partial\phi}{\partial x_i}\right|_{\boldsymbol{x}_\alpha}\Delta x_i^{(\alpha\delta)} - \frac{1}{2}\left.\frac{\partial^2\phi}{\partial x_i\partial x_j}\right|_{\boldsymbol{x}_\alpha}\Delta x_i^{(\alpha\delta)}\Delta x_j^{(\alpha\delta)}\right)}_{=(\phi|_{x_R} - \phi|_{x_L})}\end{aligned} \tag{44}$$

where the face-gradient term is approximated in a one-sided way from an extrapolated gradient of element Ω_α. The jump-term at the interface is formed with the Dirichlet boundary condition and the extrapolated face value from Ω_α. In a similar way to the inner fluxes, we could introduce additional discretization coefficients in Eq. (44) to influence the truncation errors of the scheme. However, due to the one-sided extrapolation it is not possible to achieve the same orders of accuracy for the interior faces. In fact, the use of the coefficients a, b, c from Table 1 for the fourth- and sixth-order accurate schemes in Eq. (44) even degraded the overall solution accuracy toward the case, where the equation was used without a modification. For this reason, the viscous fluxes are only calculated using Eq. (44) in this work.

III. Canonical Diffusion Problems

In this section, the influence of the proposed viscous flux formulation is verified via the following diffusion equation for a variable ϕ:

$$\frac{\partial\phi}{\partial t} = D\left(\frac{\partial^2\phi}{\partial x_1^2} + \frac{\partial^2\phi}{\partial x_2^2}\right) \tag{45}$$

which is solved in a two-dimensional computational domain $\Omega \in [0, L]\times[0, L]$ with $L = 1$ m and with various starting and boundary conditions. The test cases are used to examine the error convergence and accuracy levels of the viscous flux schemes given in Table 1. The temporal discretization of Eq. (45) is performed by a second-order accurate Crank–Nicolson scheme, which is solved with a biconjugate gradient stabilized method (BiCGSTAB) and Jacobi preconditioning. The implicit discretization of the fluxes is achieved with a deferred correction approach, so that only the volume averages $\overline{\phi}_\alpha$ and $\overline{\phi}_\beta$ in the flux equations are treated implicitly. This has the advantage that the time-consuming calculation of derivatives only has to be carried out at the beginning of a time step, whereas the temporal error and the stability are only marginally affected.

A. Two-Dimensional Diffusion of a Dirac Pulse

To verify the accuracy of the internal diffusive fluxes, a first test case is considered, where ϕ is defined as Dirac pulse $\delta(\boldsymbol{x})$ at time $t = 0$ s in the center of the domain $\boldsymbol{x}_c = [L/2, L/2]^T$, which evolves radially in time according to the following equation [31]:

$$\phi(\boldsymbol{x}, t) = \frac{1}{4\pi Dt}\exp\left(-\frac{(x_1 - x_{1,c})^2 + (x_2 - x_{2,c})^2}{4Dt}\right) \tag{46}$$

A simulation is initialized with $\phi(\boldsymbol{x}, t_1 = 1.5$ s) and is then solved up to the time $t_2 = 2.5$ s. The diffusivity $D = 10^{-4}$ m^2/s is set sufficiently small to ensure the solution is not affected by the domain boundaries, where symmetry boundary conditions are applied. This way, the influence of the latter can be neglected. A grid convergence study is performed, where the mean grid scale $h = L/\sqrt{N}$ varies between $L/20$ and $L/160$. Two different primary grid types are used—a Cartesian one, as well as an irregular triangular grid. The latter is shown exemplarily in Fig. 6 with the initial solution of the test case.

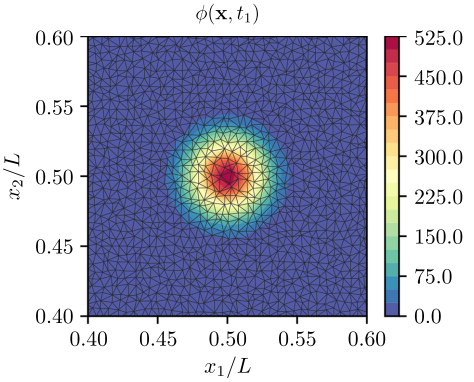

Fig. 6 Enlarged section of the initial solution for the two-dimensional diffusion of a Dirac pulse, together with the corresponding distorted primary grid structure with a mean scale of $h = L/160$.

Figure 7 shows the L^2-error norms calculated on the Cartesian (left) and the unstructured (right) grid type, where the four considered k-exact schemes are labeled according to Table 1 and the original Mathur–Murthy scheme is denoted by "*MM*". The L^2-norm is calculated from the volume-averaged solution by

$$E_{L^2}(\overline{\phi}_\alpha) = \left[\frac{\sum_{\alpha=1}^{N}(\overline{\phi}_\alpha - \overline{\phi}_\alpha^{\text{ex}})^2|\Omega_\alpha|}{\sum_{\alpha=1}^{N}|\Omega_\alpha|}\right]^{1/2} \tag{47}$$

where $\overline{\phi}_\alpha^{\text{ex}}$ is the exact solution. On the Cartesian grid type, the *EX*1-2 scheme features very similar accuracy levels to the Mathur–Murthy scheme, which has already been indicated in the analysis for the spectral properties of the schemes. With the *EX*2-2 scheme, the error is slightly reduced toward *EX*1-2 and *MM*. All three methods achieve a second-order accuracy, as predicted by the truncation error analysis. By adjusting the coefficients a, b, c accordingly, a fourth-order accuracy can be achieved with the *EX*1-4 method and a sixth-order of accuracy with the *EX*2-6 scheme. However, the results on the right of Fig. 7 indicate that these accuracy levels can no longer be obtained on the unstructured grid type, where both schemes feature similar errors to the Mathur–Murthy scheme. With the *EX*1-2 and the *EX*2-2 method, however, a second-order of accuracy is achieved despite the strong element distortion and both schemes yield similar error levels to those on the Cartesian grid.

B. Two-Dimensional Diffusion with Dirichlet Boundaries

In the next step, Eq. (45) is solved in the same computational domain as defined previously, but with the following prescribed values for ϕ at the domain boundary:

$$\begin{aligned} &\phi(x_1 = 0) = 0, \qquad \phi(x_1 = 1) = \sin(\pi x_2), \\ &\phi(x_2 = 0) = 0, \qquad \phi(x_2 = 1) = \sin(\pi x_1) \end{aligned} \tag{48}$$

so that the following stationary solution is obtained for $t \to \infty$ [32,33]

$$\phi(\boldsymbol{x}) = \frac{\sinh(\pi x_1)\sin(\pi x_2) + \sinh(\pi x_2)\sin(\pi x_1)}{\sinh(\pi)} \tag{49}$$

At the beginning of a simulation, the solution is initialized in the entire domain by $\phi(\boldsymbol{x}) = 1$. Equation (45) is then solved until the L^2 error norm of $\overline{\phi}_\alpha$ changes by less than 10^{-12} between two consecutive time steps. Again, the calculation is performed on a Cartesian and an unstructured grid, as in the previous test case. The stationary solution is shown together with the unstructured grid in Fig. 8. The results are evaluated by means of convergence study in which the mean step size $h = L/\sqrt{N}$ is successively refined from $L/20$ to $L/160$. The resulting L^2-error norms are shown in Fig. 9, where the left side corresponds to the Cartesian and the right side to the unstructured grid, respectively. On the Cartesian grid, a second-order of accuracy is obtained with the *MM*, the *EX*1-2, and the *EX*2-2 schemes. Interestingly, the *EX*1-2 scheme shows lower errors than the *EX*2-2 scheme on this grid type, even though the latter is based on a higher reconstruction level. When using the *EX*1-4 and *EX*2-6 schemes, which correspond to a modification of the discretization coefficients a, b, c at the interior fluxes, the order of accuracy collapses to a first order. This behavior can be traced back to the elements closest to the boundaries, where the element stencils do not exhibit the required symmetries due to the one-sided extrapolation in Eq. (44). As already mentioned, using the coefficients a, b, c in this boundary equation as well leads to even greater errors in both methods. On the unstructured grid, the *MM* scheme also switches to a first-order accuracy and exhibits similar error levels to the *EX*1-4 and *EX*2-6 methods. For the latter, the error levels increase compared to the Cartesian grid simulations. In contrast, both the *EX*1-2 and *EX*2-2 schemes still preserve a second-order of accuracy despite the strong element distortion, with the *EX*2-2 method now having the lowest error values. Interestingly, the *EX*2-2 scheme generates even lower error values on this grid type than on the Cartesian one. This is due to

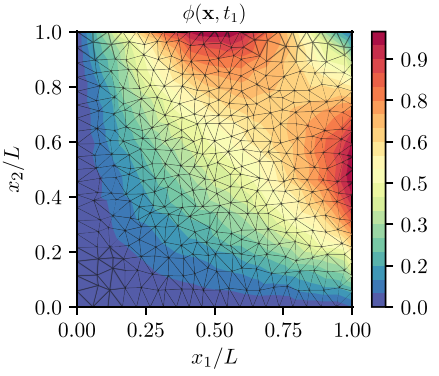

Fig. 8 Solution for the two-dimensional diffusion test case with Dirichlet boundary conditions, together with the corresponding distorted primary grid structure with a mean scale of $h = L/20$.

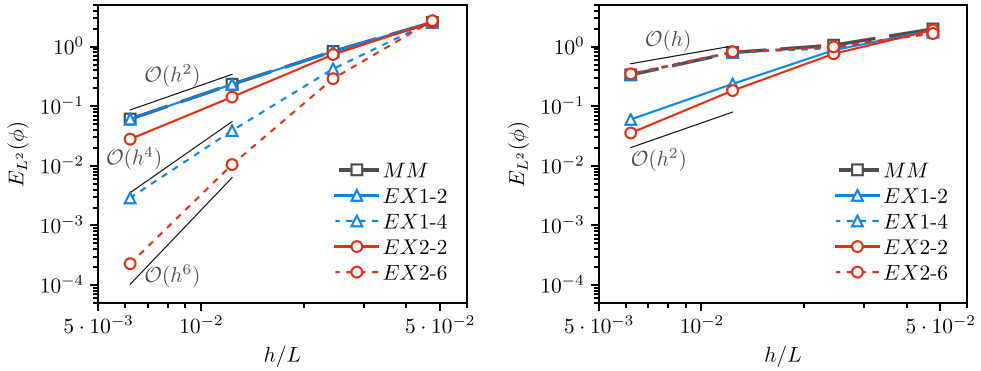

Fig. 7 Grid convergence of the L^2-error norm for the two-dimensional point source diffusion test case, calculated on the Cartesian (left) and the distorted (right) grid type.

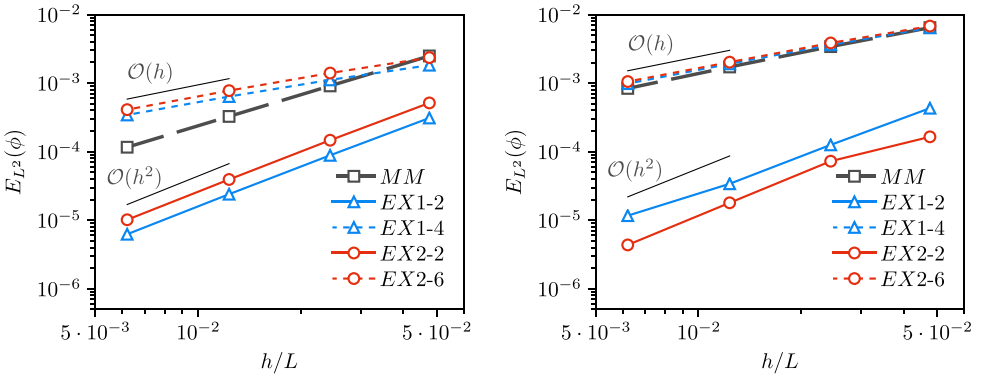

Fig. 9 Grid convergence of the L^2-error norm for the two-dimensional diffusion test case with Dirichlet boundary conditions, calculated on the Cartesian (left) and the distorted (right) grid type.

Table 2 Properties of the considered primary grids for the two-dimensional canonical diffusion problems

	Primary grid nodes	Primary grid edges	Edge/node ratio
Cartesian grids	441	840	1.904
	1681	3280	1.949
	6561	12960	1.976
	25921	51520	1.988
Distorted grids	441	1240	2.809
	1681	4880	2.899
	6561	19360	2.950
	25921	77120	2.976

the fact that the median-dual elements on the unstructured grid have a significantly higher number of direct neighboring elements, which reduces the reconstruction error. The latter can be seen from the ratios between primary grid edges and nodes, which are shown in Table 2 for the investigated computational grids. Since two median-dual elements are always connected through a primary grid edge, this ratio scales with the average number of neighboring elements in a grid.

The results confirm the previous analysis regarding the truncation error with respect to the discretization coefficients a, b, and c. On the one hand, they show that on Cartesian grids both $EX1$-4 and $EX2$-6 schemes can achieve an enormous improvement in accuracy. However, in the presence of boundary conditions or grid irregularities, the error of both variants drops to a level similar to that of the Mathur–Murthy scheme. In contrast, the error can be considerably reduced with both $EX1$-2 and $EX2$-2, regardless of the grid structure or the presence of boundary conditions. Similar results could also be confirmed for the following test cases, which is why only the two schemes $EX1$-2 and $EX2$-2 are considered in the following course of this work and compared with the conventional MM scheme.

IV. Wall-Bounded Flow Problems

For this section, we will investigate the influence of the proposed viscous flux formulation on the overall solution accuracy of wall-bounded flow problems. This requires the numerical solution to the incompressible Navier–Stokes equations

$$\frac{\partial u_i}{\partial x_i} = 0 \tag{50a}$$

$$\frac{\partial u_i}{\partial t} + \frac{\partial}{\partial x_j}(u_i u_j) - \nu \frac{\partial^2 u_i}{\partial x_j \partial x_j} = -\frac{1}{\rho}\frac{\partial p}{\partial x_i} \tag{50b}$$

with the fluid velocity $\boldsymbol{u}$, the pressure p, and the kinematic viscosity ν. A fractional step scheme is used for the pressure-velocity-coupling, which is second-order accurate in time. This involves the implicit solution of a Poisson equation for a pressure difference δp between two consecutive time steps

$$\frac{\partial^2 \delta p}{\partial x_i \partial x_i} = S_p \tag{51}$$

where S_p represents a source term that enforces a divergence constraint on the velocity field in a subsequent correction step. For a detailed description of this approach and respective extensions to enhance its accuracy with the k-exact reconstruction approach, we refer to our recent work [12,13]. It should be mentioned that besides the viscous fluxes in the momentum equations, Eq. (31) is also used to discretize the Laplacian operator in the pressure correction equation.

The scheme is implemented in DLR's in-house code **ThetaCOM**, which features a multigrid preconditioning for the Poisson equation and an efficient matrix-free Krylov solver for the system of linear equations. All test cases are simulated with a one- and a two-exact reconstruction approach, where the convective fluxes are approximated with second- and third-order accuracy, respectively. Besides that, we use the central convective flux discretization approach from our recent work [13], which minimizes the introduced amount of numerical dissipation to a minimum. As already mentioned, we will only examine the $EX1$-2 and $EX2$-2 schemes in the remainder of this paper. This is due to the fact that both the $EX1$-4 and $EX2$-6 schemes did not yield any increase in accuracy on truly unstructured grids in the previous test cases. In addition, it has also been found that both schemes have more restrictive stability constraints and may cause divergence problems, especially for grids with high aspect ratios. To assess the impact of the proposed viscous flux formulation on the spatial accuracy, the two additional schemes $EX1$-MM and $EX2$-MM are introduced. For these, the conventional Mathur–Murthy scheme is applied to both viscous and Laplace fluxes and combined with a one- and two-exact approximation of the convective fluxes, respectively.

A. Hagen–Poiseuille Flow

For the first test case, we consider a pipe of radius R with an applied axial pressure gradient G, such that a parabolic laminar flow profile emerges. The solution of this problem is given analytically by the following normalized velocity profile [34]:

$$u^+ = \frac{U_{\max}}{u_\tau}\left[1 - \left(\frac{r^+}{Re_\tau}\right)^2\right] \tag{52}$$

with the radial coordinate $r^+ = \sqrt{x_1^2 + x_2^2}/\delta_\nu$, the maximum center velocity $U_{\max} = GR^2/(4\mu)$, and the shear Reynolds number $Re_\tau = \rho u_\tau R/\mu$. The variables u_τ and δ_ν refer to the shear velocity and the wall length scale. The parameters are chosen to $G = 0.48$ Pa/m, $\mu = 0.01$ Pa $\cdot$ s, $\rho = 1.0$ kg/m^3, and $R = 0.5$ m, which gives $Re_\tau \approx 173$, $\delta_\nu \approx 2.886$ mm, and $u_\tau \approx 3.464$ m/s. Several simulations are conducted where the pipe cross section is discretized as shown by the median-dual representation in Fig. 10. We apply a no-slip wall condition at the outer boundary of the pipe, whereas a periodic boundary condition is applied in the axial direction. In this way it is possible to compute the problem with only two element layers in the axial direction, which significantly reduces the computational effort. Several

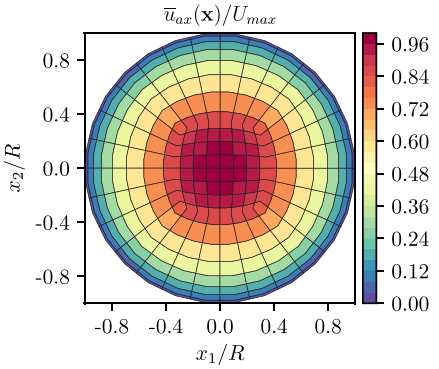

Fig. 10 Normalized axial velocity field for the Hagen–Poiseuille flow and a considered grid for the numerical simulation with a mean grid width $h^+ = 1.63$ and 390 median-dual elements.

Table 3 Grid properties for the Hagen–Poiseuille flow

Grid	N	$h^+_{\text{rad},1}$	$h^+_{\text{tan},1}$	h^+
1	78	1.79	9.07	3.55
2	390	0.57	3.89	1.63
3	1734	0.24	1.81	0.76
4	7302	0.12	0.88	0.37
5	29958	0.06	0.43	0.18

Given are the number of nodes N in the x_1–x_2 plane, the radial and tangential grid widths $h^+_{\text{rad},1}$ and $h^+_{\text{tan},1}$, as well as the mean grid width h^+ along the entire radius.

grid refinement levels are used, which are given in Table 3. For all simulations, the flow field is initialized with $\boldsymbol{u} = 0$ and the axial pressure gradient is applied to the momentum equations as a source term, thus leading to the emergence of a steady laminar flow profile.

Figure 11 shows the normalized volume-averaged velocity profiles that are calculated with the considered schemes and a mean grid width $h^+ = 1.63$, which refers to the second grid in Table 3. It can be observed that the proposed formulation generally enhances the accuracy of the simulated profiles for both discretization schemes, even though the increase in accuracy is greater when combined with a two-exact reconstruction. This result is supported by the L^2-norm of the volume-averaged flow field, shown in Fig. 12 for the volume-averaged axial velocity $E_{L^2}(\bar{u}_{\text{ax}})$, as well as for the axial velocity gradient $E_{L^2}(\partial u_{\text{ax}}/\partial x_1)$. All presented schemes preserve a second-order accurate convergence of $E_{L^2}(\bar{u}_{\text{ax}})$. The results imply for the two-exact schemes that the error convergence of its third-order accurate convective operator is deteriorated by the second-order accurate diffusive operator. This is probably related to the fact that the error terms of the viscous fluxes dominate over the convective fluxes due to the low Reynolds number of the flow. However, when using the $EX2$-2 or $EX1$-2 scheme, the error in the prediction of $\bar{u}_{\text{ax}}$ is reduced by at least one order of magnitude and the error in the axial velocity gradient is even reduced by almost two orders of magnitude. It can also be observed that the errors of the solution gradients collapse to a first-order accuracy when the Mathur–Murthy scheme is used, whereas otherwise it features a second-order accuracy. However, for the $EX2$-2 scheme the second-order accuracy of $E_{L^2}(\partial u_{\text{ax}}/\partial x_1)$ reduces to $\mathcal{O}(h)$ as the curve falls below a certain threshold of $h^+ \approx 8 \cdot 10^{-5}$. This can be explained by the fact that the gradient approximation is based on volume averages that exhibit an error of $\mathcal{O}(h^2)$. This error is cascaded in the gradient approximation via Eqs. (8) and (9) and thus manifests itself with $\mathcal{O}(h)$ in the gradient field. But because this first-order error is comparatively small, it only appears below the aforementioned threshold.

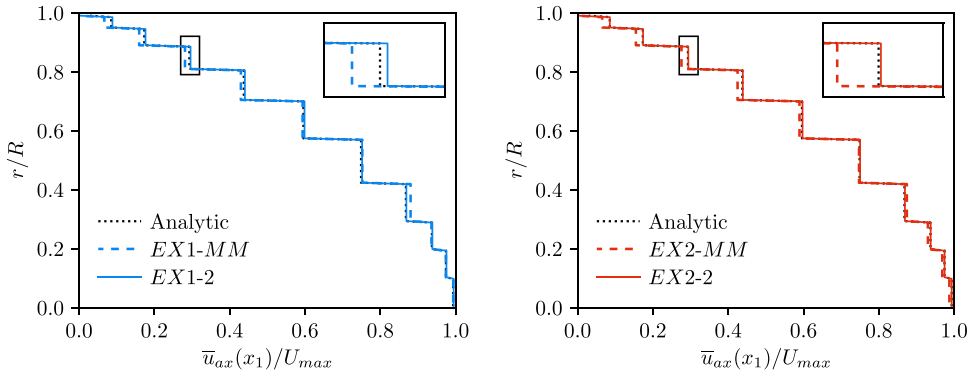

Fig. 11 Normalized axial flow profiles for the Hagen–Poiseuille test case, calculated with a mean grid width $h^+ = 1.63$, 390 median-dual elements, and for both one- and two-exact schemes.

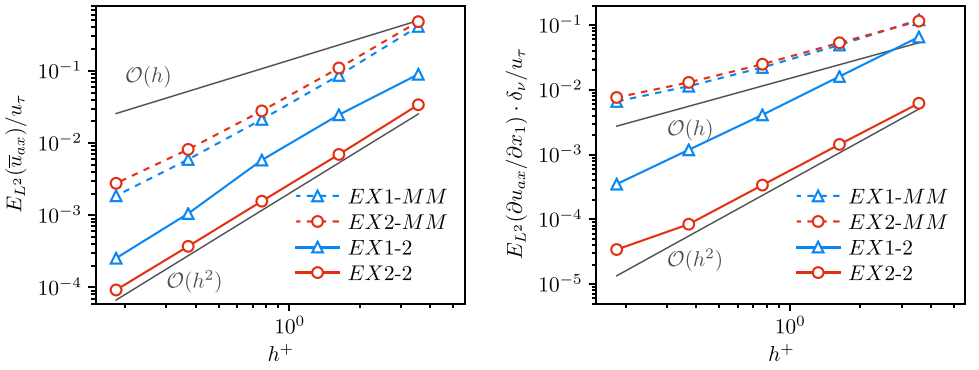

Fig. 12 Grid convergence study for the L^2-error of the volume-averaged axial velocity $\bar{u}_{\text{ax}}$ and for the axial velocity gradient $\partial u_{\text{ax}}/\partial x_1|_{x_a}$ of the Hagen–Poiseuille flow, calculated for both one- and two-exact schemes.

B. Laminar Cylinder Flow

This test case has been proposed by Schäfer et al. [35] in the workshop *Flow Simulation with High-Performance Computers*. It has already been used in a prior work [12] to verify the accuracy properties of the proposed k-exact reconstruction scheme, but due to stability reasons with a reduced reconstruction order in boundary elements. Furthermore, no clear distinction was made between the contributions of convective and diffusive flux corrections on the solution accuracy. These issues will be addressed in the following by investigating the influence of the viscous flux discretization on the solution in a way similar to the previous test case. The flow of an incompressible fluid around a cylindrical obstacle of diameter $D = 0.1$ m within a channel of size 2.2 m $\times$ 0.41 m at Reynolds number of $Re = 100$ is conducted. The latter is based on the cylinder's diameter. The obstacle experiences a periodic change in drag and lift force as a result of the downstream vortex shedding. The aim of the simulations is to predict the resulting maxima in the cylinder's drag and lift coefficients $C_{D,\max}$ and $C_{L,\max}$, as well as the frequency f of these oscillations. The latter is characterized by the Strouhal number $St = Df/U$ which is based on cylinder diameter D and the mean flow velocity $U = 1.0$ m/s. For a detailed overview of the test case and the actual definition of $C_{D,\max}$ and $C_{L,\max}$, we refer to the work by Schäfer et al. [35]. The simulation is conducted on five meshes with varying numbers of primary grid vertices $N = \{2753, 5583, 10887, 22152, 43332\}$. The meshes consist of triangular elements, and, apart from the cylinder curvature, there is no significant refinement of the elements in the vicinity of walls. The coarsest mesh is shown in Fig. 13 by means of its median-dual representation. At the beginning of a simulation run, the velocity field is initialized with $\boldsymbol{u} = 0$. Subsequently the time-dependent Navier–Stokes equations (50a) and (50b) are solved for a simulation time of 8 s with a Courant number of approximately 0.4.

Figure 14 shows the calculated flow field by means of the absolute velocity and the vorticity. The solution stems from the two-exact scheme on a grid with 10887 primary grid vertices during the state of maximum lift and with the utilization of the viscous flux correction. The actual influence of the viscous flux scheme on the target variables $C_{D,\max}$, $C_{L,\max}$, and St is shown in Fig. 15 by means of a grid

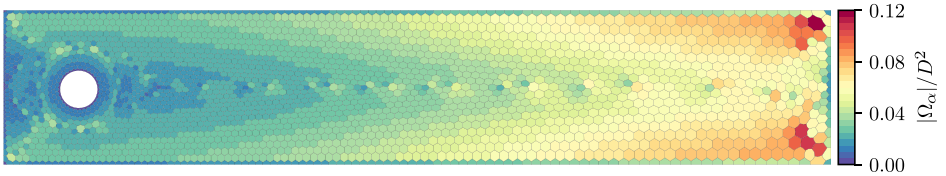

Fig. 13 Median-dual grid for the laminar cylinder flow problem with 2753 elements, colored by the normalized element size $|\Omega_\alpha|/D^2$.

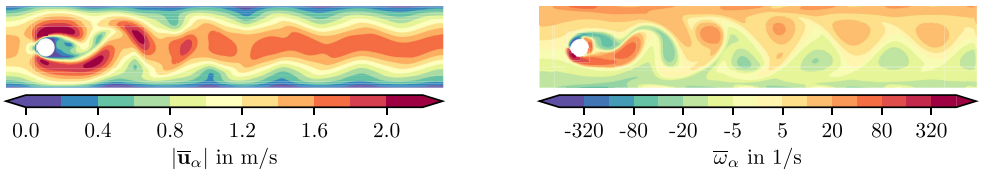

Fig. 14 Contours of the absolute volume-averaged velocity $|\bar{u}_\alpha|$ and vorticity $\bar{\omega}_\alpha$ for the laminar cylinder flow problem with 10,887 vertices, calculated with the *EX*2-2 scheme.

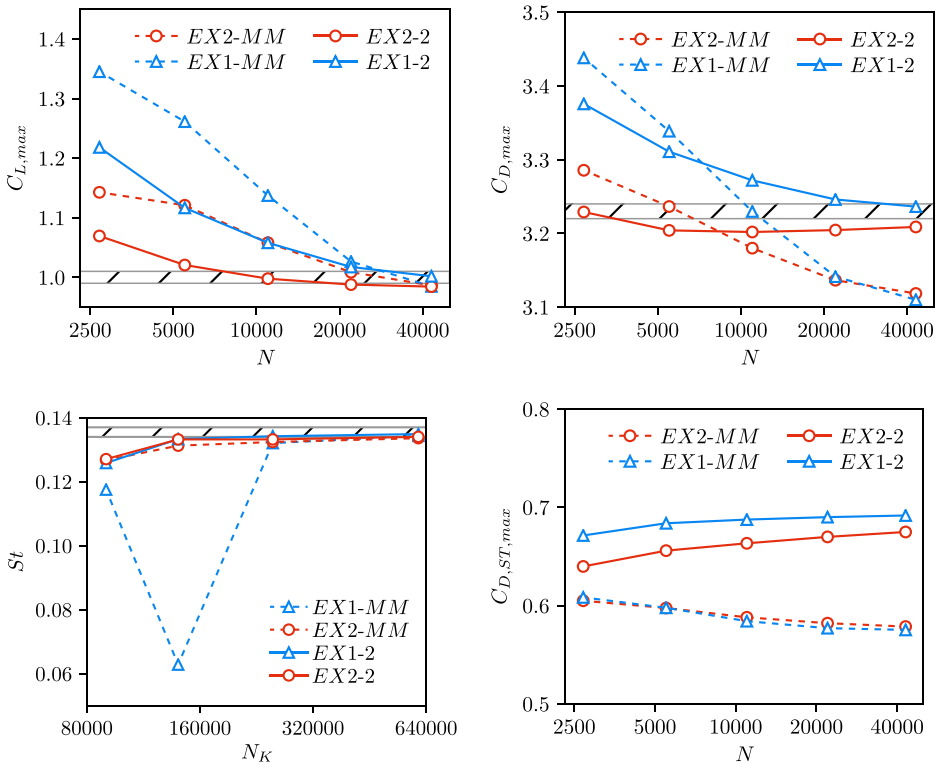

Fig. 15 Grid convergence study results for the laminar cylinder test case. The dashed areas correspond to reference values given by Schäfer et al. [35].

convergence study. Clearly, using the $EX2$-2 and $EX1$-2 schemes results in a more accurate approximation of the maximum lift and drag coefficient $C_{D,\max}$ and $C_{L,\max}$, whereas the Strouhal number is less affected by the choice of the viscous flux discretization. In particular for the $EX2$-2 scheme, both $C_{D,\max}$ and $C_{L,\max}$ are approximated with a reasonable accuracy at $N = 10887$ nodes. On the other hand, using the Mathur–Murthy scheme causes the maximum drag coefficient to converge toward too low values. This indicates that it is necessary to maintain the underlying k-exact reconstruction for both convective and diffusive fluxes in order to achieve accurate simulation results. This becomes particularly clear in the comparison between $EX1$-2 and $EX1$-MM, as these methods only differ in the calculation of the jump-terms of Eqs. (31) and (44). In the $EX1$-MM scheme, the latter is simply calculated from volume averages, whereas, for $EX1$-2, a conversion to point values is carried out via Eq. (12). Figure 15 also shows the shear stress contribution of the maximum drag coefficient, which is denoted by $C_{D,ST,\max}$. The latter varies only marginally with N, and, with regard to $C_{D,\max}$, the results of the all schemes for $C_{D,ST,\max}$ only differ by a few percent. This suggests that the improvements in $C_{D,\max}$ with $EX2$-2 and $EX1$-2 are mainly attributed to the pressure contribution and hence to the modified Laplace operator in the pressure-correction equation (51) of the fractional step method.

C. Laminar Flow Around a Sphere

For this test case, we consider a sphere of radius $R = 1$ mm in a rectangular domain of size 120 mm × 30 mm × 30 mm. The latter consists of an inlet, an outlet, and four symmetry boundary conditions. The sphere, whose surface is modeled by means of a no-slip boundary condition, is surrounded by a flow at $Re = 300$ based on the sphere's diameter, at which a characteristic shedding of hairpin-shaped vortices occurs in its wake. This phenomenon is described in detail in the work of Johnson and Patel [36] and is depicted exemplarily in Fig. 16 by means of the λ_2 vortex criterion [37], where a value of $\lambda_2 = -100$ is selected to represent the isocontours. The sphere is placed 20 mm downstream from the domain's inlet boundary condition. For the demonstration of the proposed viscous flux discretization, four fully unstructured grids are considered, which consist of prismatic and tetrahedral elements and which vary in their number of primary grid vertices by $N = \{92381, 139589, 252101, 610159\}$. The prismatic elements are used to account for the sphere's boundary layer. Figure 17 shows the mesh with $N = 139589$ vertices. The velocity field is initialized with $\boldsymbol{u} = \boldsymbol{0}$, followed by the flow simulation for a time of 0.88 s. The time step size is based on the grid so that a CFL number of $\sigma \approx 0.2$ is achieved. To validate the solution, the temporal variation of the drag coefficient C_D and the lateral force coefficient C_L are calculated, which result from the corresponding surface forces on the sphere due to the vortical structures. Here, the lateral component is defined as the force that is acting in the direction of the symmetry plane of the vortical structures in the wake of the sphere.

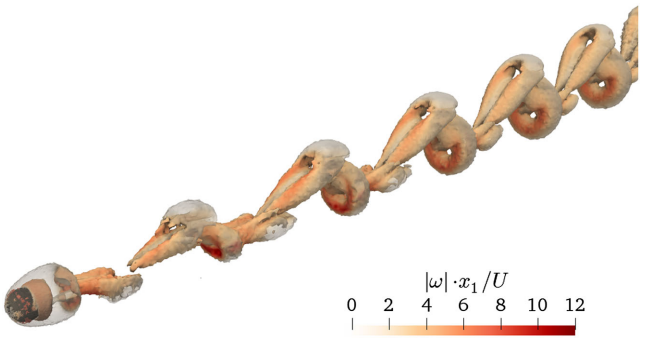

Fig. 16 Vortex structures of the laminar flow around a sphere, represented by the λ_2 vortex criterion and colored by the vorticity magnitude $|\omega|$, which is scaled by the x_1 distance to the sphere and the ambient velocity U. The results correspond to the $EX2$-2 scheme and the finest grid with 610,159 vertices.

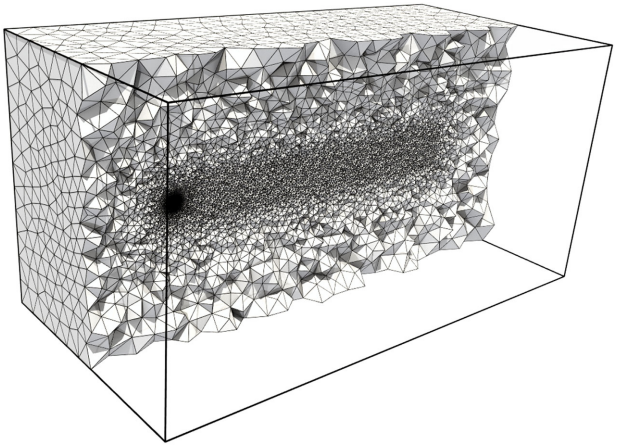

Fig. 17 Primary grid structure with 139,589 vertices for the laminar flow around a sphere at $Re = 300$.

The quality of the simulations is assessed on the basis of the mean drag coefficient $C_{D,m}$, the amplitudes of both drag and lateral force coefficient $C_{D,amp}$ and $C_{L,amp}$, as well as the Strouhal number St, which is calculated from the frequency of the drag force. Figure 18 shows these target quantities as a function of the number of primary grid vertices of the four considered grids and the four considered discretization schemes. The dashed areas correspond to reference values from the literature [36,38–40], which are used to assess the simulation results. For the $EX1$-MM scheme, an outlier in the Strouhal number and in $C_{D,amp}$ can be observed for the grid with 139,589 nodes, which is due to errors caused by the strong grid anisotropy. A sufficient accuracy for all four target quantities can only be obtained on the finest grid with this scheme. With the $EX2$-MM scheme no outliers are present, but the amplitudes of both coefficients C_D and C_L are underestimated on all grids. In comparison, all four target variables can be accurately predicted with methods $EX2$-1 and $EX2$-2 on the much coarser grids. This can be seen in particular for the mean value of the drag coefficient $C_{D,m}$.

V. Conclusion

In this work, a formulation for the discretization of viscous fluxes at interior faces and at Dirichlet boundaries in the scope of k-exact schemes and unstructured median-dual grids was proposed. The approach has been incorporated in conjunction with the k-exact multiple-correction method for vertex-centered grids of the DLR in-house code **ThetaCOM**. Similar to various viscous flux schemes for the unstructured finite-volume method, for example, the approach by Mathur and Murthy [17], the proposed scheme is based on a geometric decomposition of the viscous flux into parts that are orthogonal and nonorthogonal to the flux surface. It is shown that the introduction of additional discretization coefficients can be used to connect this decomposition approach to the well-known α-damping scheme [16] for viscous fluxes, which is derived from a fist-order hyperbolic relaxation system for diffusion. The introduced coefficients act as degrees of freedom for the numerical properties of the scheme, which has been analyzed in terms of both the truncation error and the spectral properties. An analogy to the α-damping scheme was also shown for the viscous flux calculation at Dirichlet boundaries, although no additional discretization coefficients were introduced here.

By means of canonical diffusion test cases, it has been shown that special coefficients can achieve fourth- or sixth-order accuracy on Cartesian grids when combined with a one-exact or two-exact reconstruction, respectively. However, on truly unstructured grids or in the presence of Dirichlet boundary conditions, these accuracy levels collapsed to similar error thresholds as achieved with the conventional scheme by Mathur and Murthy, which has also been taken into consideration. On the other side, when using the initial

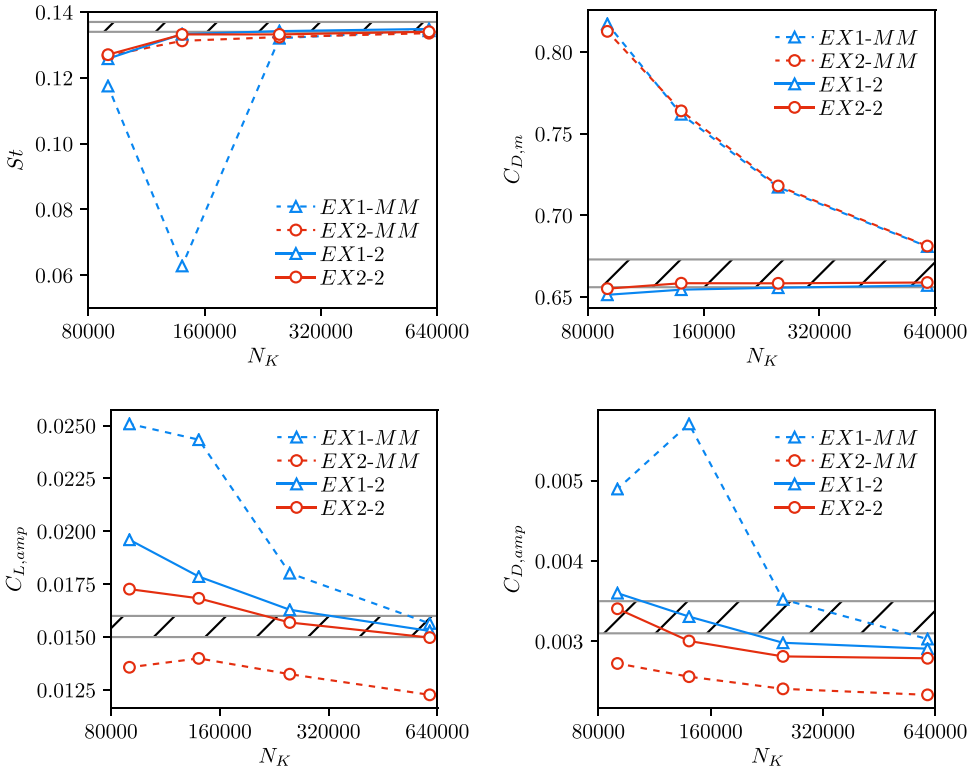

Fig. 18 Target values for the laminar flow around a sphere as a function of primary grid vertices. The dashed areas correspond to reference values from the literature [36,38–40].

discretization coefficients that stem from a perspective of the k-exact reconstruction framework, the proposed method is capable to reduce the numerical error toward the conventional scheme with a second order of accuracy on both Cartesian and irregular meshes as well as in the presence of Dirichlet boundaries. Considering these results, the latter approach has been investigated in three wall-bounded, laminar flow problems: a steady Hagen–Poisseuille flow in a pipe, a laminar cylindrical flow in $2D$, and a laminar flow around a sphere in $3D$. Again, simulations with the conventional Mathur–Murthy scheme have been performed for comparison. For all three test cases, the proposed method was able to accurately predict various target variables on coarser grids and with a greater independence from the underlying grid structure than the conventional method. The most accurate results were obtained when combining a two-exact reconstruction with the proposed viscous flux formulation at both interior and boundary faces.

In future work, it should be investigated how the proposed flux formulation affects other diffusion-driven flow problems, for example, in laminar flames with multispecies transport. Furthermore, it should be examined whether the introduced discretization coefficients can be varied locally in hybrid grids on the basis of certain grid metrics in order to realize fourth- or sixth-order accuracy for the viscous operator in selected regions of complex geometries.

Acknowledgement

The authors gratefully acknowledge the scientific support and HPC resources provided by the German Aerospace Center (DLR). The HPC system CARO is partially funded by "Ministry of Science and Culture of Lower Saxony" and "Federal Ministry for Economic Affairs and Climate Action". We would also like to thank Dr.-Ing. A. Fiolitakis for the helpful discussions on this work.

References

[1] Ekaterinaris, J. A., "High-Order Accurate, Low Numerical Diffusion Methods for Aerodynamics," *Progress in Aerospace Sciences*, Vol. 41, Nos. 3–4, 2005, pp. 192–300. https://doi.org/10.1016/j.paerosci.2005.03.003

[2] Cockburn, B., and Shu, C.-W., "TVB Runge-Kutta Local Projection Discontinuous Galerkin Finite Element Method for Conservation Laws. II. General Framework," *Mathematics of Computation*, Vol. 52, No. 186, 1989, pp. 411–435. https://doi.org/10.1090/S0025-5718-1989-0983311-4

[3] Cockburn, B., Lin, S.-Y., and Shu, C.-W., "TVB Runge-Kutta Local Projection Discontinuous Galerkin Finite Element Method for Conservation Laws III: One-Dimensional Systems," *Journal of Computational Physics*, Vol. 84, No. 1, 1989, pp. 90–113. https://doi.org/10.1016/0021-9991(89)90183-6a

[4] Cockburn, B., Hou, S., and Shu, C.-W., "The Runge-Kutta Local Projection Discontinuous Galerkin Finite Element Method for Conservation Laws. IV. The Multidimensional Case," *Mathematics of Computation*, Vol. 54, No. 190, 1990, pp. 545–581. https://doi.org/10.1090/S0025-5718-1990-1010597-0

[5] Cockburn, B., and Shu, C.-W., "The Runge-Kutta Discontinuous Galerkin Method for Conservation Laws V: Multidimensional Systems," *Journal of Computational Physics*, Vol. 141, No. 2, 1998, pp. 199–224. https://doi.org/10.1006/jcph.1998.5892

[6] Wang, Z. J., "Spectral (finite) Volume Method for Conservation Laws on Unstructured Grids: Basic Formulation," *Journal of Computational Physics*, Vol. 178, No. 1, 2002, pp. 210–251. https://doi.org/10.1006/jcph.2002.7041

[7] Wang, Z. J., Liu, Y., and Kwak, D., "Spectral (finite) Volume Method for Conservation Laws on Unstructured Grids II: Extension to Two Dimensional Scalar Equation," *Journal of Computational Physics*, Vol. 179, No. 2, 2002, pp. 665–697. https://doi.org/10.1006/jcph.2002.7082

[8] Wang, Z. J., and Liu, Y., "Spectral (finite) Volume Method for Conservation Laws on Unstructured Grids III: One Dimensional Systems and Partition Optimization," *Journal of Scientific Computing*, Vol. 20, No. 1, 2004, pp. 137–157. https://doi.org/10.1023/A:1025896119548

[9] Wang, Z. J., Zhang, L., and Liu, Y., "Spectral (finite) Volume Method for Conservation Laws on Unstructured Grids IV: Extension to Two-Dimensional Systems," *Journal of Computational Physics*, Vol. 194, No. 2, 2004, pp. 716–741. https://doi.org/10.1016/j.jcp.2003.09.012

[10] Pont, G., Brenner, P., Cinnella, P., Maugars, B., and Robinet, J.-C., "Multiple-Correction Hybrid k-Exact Schemes for High-Order

Compressible RANS-LES Simulations on Fully Unstructured Grids," *Journal of Computational Physics*, Vol. 350, Dec. 2017, pp. 45–83. https://doi.org/10.1016/j.jcp.2017.08.036

[11] Menasria, A., Brenner, P., Cinnella, P., and Pont, G., "Toward an Improved Wall Treatment for Multiple-Correction k-Exact Schemes," *2018 Fluid Dynamics Conference*, AIAA Paper 2018-4164, 2018. https://doi.org/10.2514/6.2018-4164

[12] Setzwein, F., Ess, P., and Gerlinger, P., "An Implicit High-Order k-Exact Finite-Volume Approach on Vertex-Centered Unstructured Grids for Incompressible Flows," *Journal of Computational Physics*, Vol. 446, Dec. 2021, Paper 110629. https://doi.org/10.1016/j.jcp.2021.110629

[13] Setzwein, F., Ess, P., and Gerlinger, P., "Adaptive Numerical Dissipation Control for High-Order k-Exact Reconstruction Schemes on Vertex-Centered Unstructured Grids Using Artificial Neural Networks," *Journal of Computational Physics*, Vol. 471, Dec. 2022, Paper 111633. https://doi.org/10.1016/j.jcp.2022.111633

[14] Chamarthi, A. S., Bokor, S., and Frankel, S. H., "On the Importance of High-Frequency Damping in High-Order Conservative Finite-Difference Schemes for Viscous Fluxes," *Journal of Computational Physics*, Vol. 460, July 2022, Paper 111195. https://doi.org/10.1016/j.jcp.2022.111195

[15] Chamarthi, A. S., Chandravamsi, H., Hoffmann, N., Bokor, S., and Frankel, S. H., "On the Role of Spectral Properties of Viscous Flux Discretization for Flow Simulations on Marginally Resolved Grids," *Computers & Fluids*, Vol. 251, Jan. 2023, Paper 105742. https://doi.org/10.1016/j.compfluid.2022.105742

[16] Nishikawa, H., "Beyond Interface Gradient: A General Principle for Constructing Diffusion Schemes," *40th Fluid Dynamics Conference and Exhibit*, AIAA Paper 2010-5093, 2010. https://doi.org/10.2514/6.2010-5093

[17] Mathur, S., and Murthy, J., "A Pressure-Based Method for Unstructured Meshes," *Numerical Heat Transfer*, Vol. 31, No. 2, 1997, pp. 195–215. https://doi.org/10.1080/10407799708915105

[18] Setzwein, F., Ess, P., and Gerlinger, P., "High-Order k-Exact Finite Volume Scheme for Vertex-Centered Unstructured Grids," *AIAA Scitech 2020 Forum*, AIAA Paper 2020-1785, 2020. https://doi.org/10.2514/6.2020-1785

[19] Setzwein, F., Spraul, M., Ess, P., and Gerlinger, P. M., "On the Structure of Correction Matrices for a k-Exact High-Order Finite-Volume Scheme on Vertex-Centered Unstructured Grids," *AIAA Scitech 2021 Forum*, AIAA Paper 2021-1548, 2021. https://doi.org/10.2514/6.2021-1548

[20] Barth, T., and Frederickson, P., "Higher Order Solution of the Euler Equations on Unstructured Grids Using Quadratic Reconstruction," *28th Aerospace Sciences Meeting*, AIAA Paper 1990-0013, 1990. https://doi.org/10.2514/6.1990-13

[21] Ollivier-Gooch, C. F., "Quasi-ENO Schemes for Unstructured Meshes Based on Unlimited Data-Dependent Least-Squares Reconstruction," *Journal of Computational Physics*, Vol. 133, No. 1, 1997, pp. 6–17. https://doi.org/10.1006/jcph.1996.5584

[22] Ollivier-Gooch, C., and Van Altena, M., "A High-Order-Accurate Unstructured Mesh Finite-Volume Scheme for the Advection-Diffusion Equation," *Journal of Computational Physics*, Vol. 181, No. 2, 2002, pp. 729–752. https://doi.org/10.1006/jcph.2002.7159

[23] Charest, M. R., Canfield, T. R., Morgan, N. R., Waltz, J., and Wohlbier, J. G., "A High-Order Vertex-Based Central ENO Finite-Volume Scheme for Three-Dimensional Compressible Flows," *Computers & Fluids*, Vol. 114, July 2015, pp. 172–192. https://doi.org/10.1016/j.compfluid.2015.03.001

[24] Nishikawa, H., "A Face-Area-Weighted 'Centroid' Formula for Finite-Volume Method that Improves Skewness and Convergence on Triangular Grids," *Journal of Computational Physics*, Vol. 401, Jan. 2020, Paper 109001. https://doi.org/10.1016/j.jcp.2019.109001

[25] Nishikawa, H., "A Hyperbolic Poisson Solver for Tetrahedral Grids," *Journal of Computational Physics*, Vol. 409, May 2020, Paper 109358. https://doi.org/10.1016/j.jcp.2020.109358

[26] Thomas, J. L., Diskin, B., and Nishikawa, H., "A Critical Study of Agglomerated Multigrid Methods for Diffusion on Highly-Stretched Grids," *Computers & Fluids*, Vol. 41, No. 1, 2011, pp. 82–93. https://doi.org/10.1016/j.compfluid.2010.09.023

[27] Demirdžić, I., "On the Discretization of the Diffusion Term in Finite-Volume Continuum Mechanics," *Numerical Heat Transfer, Part B: Fundamentals*, Vol. 68, No. 1, 2015, pp. 1–10. https://doi.org/10.1080/10407790.2014.985992

[28] Muzaferija, S., and Gosman, D., "Finite-Volume CFD Procedure and Adaptive Error Control Strategy for Grids of Arbitrary Topology," *Journal of Computational physics*, Vol. 138, No. 2, 1997, pp. 766–787. https://doi.org/10.1006/jcph.1997.5853

[29] Demirdžić, I., and Muzaferija, S., "Numerical Method for Coupled Fluid Flow, Heat Transfer and Stress Analysis Using Unstructured Moving Meshes with Cells of Arbitrary Topology," *Computer Methods in Applied Mechanics and Engineering*, Vol. 125, Nos. 1–4, 1995, pp. 235–255. https://doi.org/10.1016/0045-7825(95)00800-G

[30] Jasak, H., "Error Analysis and Estimation for the Finite Volume Method with Applications to Fluid Flows," Ph.D. Thesis, Imperial College London, London, England, 1996.

[31] Pattle, R., "Diffusion from an Instantaneous Point Source with a Concentration-Dependent Coefficient," *Quarterly Journal of Mechanics and Applied Mathematics*, Vol. 12, No. 4, 1959, pp. 407–409. https://doi.org/10.1093/qjmam/12.4.407

[32] Nishikawa, H., "A First-Order System Approach for Diffusion Equation. I: Second-Order Residual-Distribution Schemes," *Journal of Computational Physics*, Vol. 227, No. 1, 2007, pp. 315–352. https://doi.org/10.1016/j.jcp.2007.07.029

[33] Nishikawa, H., "First-, Second-, and Third-Order Finite-Volume Schemes for Diffusion," *Journal of Computational Physics*, Vol. 256, Jan. 2014, pp. 791–805. https://doi.org/10.1016/j.jcp.2013.09.024

[34] Schlichting, H., and Gersten, K., *Grenzschicht-Theorie*, Springer, Berlin, 2006, pp. 117–118. https://doi.org/10.1007/3-540-32985-4

[35] Schäfer, M., Turek, S., Durst, F., Krause, E., and Rannacher, R., "Benchmark Computations of Laminar Flow Around a Cylinder," *Flow Simulation with High-Performance Computers II*, Springer, Berlin, 1996, pp. 547–566. https://doi.org/10.1007/978-3-322-89849-4_39

[36] Johnson, T., and Patel, V., "Flow Past a Sphere Up to a Reynolds Number of 300," *Journal of Fluid Mechanics*, Vol. 378, Jan. 1999, pp. 19–70. https://doi.org/10.1017/S0022112098003206

[37] Jeong, J., and Hussain, F., "On the Identification of a Vortex," *Journal of Fluid Mechanics*, Vol. 285, Jan. 1995, pp. 69–94. https://doi.org/10.1017/S0022112095000462

[38] Gassner, G. J., Lörcher, F., Munz, C.-D., and Hesthaven, J. S., "Polymorphic Nodal Elements and Their Application in Discontinuous Galerkin Methods," *Journal of Computational Physics*, Vol. 228, No. 5, 2009, pp. 1573–1590. https://doi.org/10.1016/j.jcp.2008.11.012

[39] Kim, J., Kim, D., and Choi, H., "An Immersed-Boundary Finite-Volume Method for Simulations of Flow in Complex Geometries," *Journal of Computational Physics*, Vol. 171, No. 1, 2001, pp. 132–150. https://doi.org/10.1006/jcph.2001.6778

[40] Tomboulides, A., Orszag, S., and Karniadakis, G., "Direct and Large-Eddy Simulations of Axisymmetric Wakes," *31st Aerospace Sciences Meeting*, AIAA Paper 1993-0546, 1993. https://doi.org/10.2514/6.1993-546

K. Taira
Associate Editor